

CZECH TECHNICAL UNIVERSITY IN PRAGUE
FACULTY OF NUCLEAR SCIENCE AND PHYSICAL
ENGINEERING

Diploma Thesis

Muon trigger efficiency of the ATLAS
Detector at LHC

Prague, 2010

Author: Petr Gallus

Prohlášení

Prohlašuji, že jsem svou diplomovou práci vypracoval samostatně a použil jsem pouze podklady uvedené v příloženém seznamu.

V Praze dne _____

podpis

Acknowledgements

I would like to thank my supervisor Vaclav Vrba for support during my studies. Also I would like to express my thanks to Michal Marcisovsky for valuable advice and discussions. I thank to Kunihiro Nagano, the speaker of Muon Identification Group, for introduction to the data analysis and structure of data samples.

Abstrakt

Tato práce je věnována studiu efektivity mionového triggeru v experimentu ATLAS na urychlovači LHC. Obsahuje měření efektivity triggerů z první (LVL1) a druhé úrovně (LVL2) mionového triggeru. Effektivitu triggerů z LVL1 měříme pomocí dat z Monte-Carlo simulace pro L1_MU20 a L1_2MU20 trigger. Pro LVL2 je analyzována efektivita MuFast triggeru v závislosti na rozhodnutí LVL1 triggeru. Výsledky ukazují, že v obou případech efektivita triggeru závisí na geometrii detektoru a příčné hybnosti p_T vylétávajících mionů.

Klíčová slova: ATLAS, LHC, trigger

Abstract

The diploma thesis is devoted to the study of the muon trigger efficiency performance in the ATLAS experiment at the LHC collider. It contains measurements of efficiency of muon triggers of Level 1 and Level 2. Level 1 (LVL1) trigger efficiency of L1_MU20 and L1_2MU20 triggers is measured using Monte-Carlo simulated events. For Level 2 the efficiency of MuFast trigger is analysed in relation to the LVL1 decision. In both examples it is shown that the trigger efficiency depends on the detector geometry and transversal momentum p_T of muons.

Key words: ATLAS, LHC, trigger

Contents

1	Actual problems in high energy physics	1
1.1	Introduction	1
1.2	The standard model in particle physics	2
1.3	The Feynman calculus and cross section	4
1.4	CP-Violation	5
1.5	Muon interaction with detector material	5
2	The Large Hadron Collider and detector ATLAS	9
2.1	The LHC	9
2.2	The ATLAS experiment	11
2.2.1	Overall design	11
2.2.2	The Inner Detector (ID)	13
2.2.2.1	Pixel Detector	13
2.2.2.2	SemiConductor Tracker(SCT)	14
2.2.2.3	Transition Radiation Tracker (TRT)	14
2.2.3	The ElectroMagnetic Calorimeter (EM calorimeter)	14
2.2.4	The Hadronic Calorimeter	15
2.2.5	The Magnet system	15
2.2.6	The Muon Spectrometer	16
2.2.6.1	Monitored Drift Tube Chambers (MDTs)	17
2.2.6.2	Cathode Strip Chambres (CSCs)	18
2.2.6.3	Resistive Plate Chambers (RPCs)	18
2.2.6.4	Thin Gap Chambres (TGCs)	19
3	Trigger	21
3.1	Level 1 trigger (LVL1)	23
3.2	Level 2 trigger (LVL2)	24

3.3	Event Filter (EF)	25
3.4	Muon triggers	25
3.4.1	Level-1 muon trigger	25
3.4.2	Level-2 muon trigger	27
3.4.2.1	MuFast algorithm	28
3.4.2.1.1	Pattern recognition	29
3.4.2.1.2	Track fit	30
3.4.2.1.3	p_T estimate	30
4	Data analysis	33
4.1	Data samples	33
4.2	Level 1 efficiencies	34
4.2.1	Event distribution	35
4.2.2	L1_MU20 item	36
4.2.3	L1_2MU20 item	38
4.3	MuFast efficiency	40
4.3.1	Event distribution	40
4.3.2	Efficiency of MuFast in dependence of LVL1 decision	42
5	Conclusion	45

Chapter 1

Actual problems in high energy physics

1.1 Introduction

Subject of this diploma thesis is muon trigger and it's efficiency at the ATLAS experiment situated at interaction point at the Large Hadron Collider (LHC). In the beginning we should take in consideration of another emerging question, that is why we need muon trigger or why are events with muons important and interesting.

Muons were discovered by Carl D. Anderson and Seth Neddermeyer at Caltech in 1936 in cosmic ray tracks. They studied track from cosmic radiation in magnetic field and they discovered particle with track more curved than proton and less than electron with similar momentum. From premise that it has equal charge as electron they assumed that this particle has mass between electron and proton. It was called mesotron, lately meson and after the discovery of π mesons it was renamed the μ meson. And at last this particle was rename to the muon, when it was discovered that it isn't meson but a lepton.

Muon has special position in the group of elementary particles. It has well known mass of 105.7 MeV, which is much larger than electron. It causes that muon loses energy mostly by ionization of material and with it's mean lifetime of 2.2 μ s it can traverse intact through most of today's experiments in high energy physics. Muons are also easy to be detected as all charged particles. That property implies that for di-lepton decays of neutral particles such as Z boson or J/ψ the muon channel allows very good measurement of invariant mass and other properties[1,2].

1.2 The standard model in particle physics

The standard model is a mixture of quantum field theory and gauge symmetries. It describes the interactions between all known particles. From contemporary experiments we know that the world around us consists of twelve elementary fermions (particles with spin $1/2$) and their anti-particles. They can be divided into two groups in dependence on preferred interaction. These groups are :

- quarks – interact by strong, weak and electromagnetic interaction
- leptons – don't interact by strong interaction

These two groups consist of three generations (families).

We also know four fundamental forces and their carriers (bosons – particles with integral spin).

- Strong force – 8 gluons g_i
- Weak force – neutral boson Z , charged bosons W^+ , W^-
- Electromagnetic force - photon
- gravitational force - hypothetical spin 2 graviton

An overview of all fermions and bosons and their charge properties is given in table 1.1, where Q represents charge, I^W spin and I_3^W value of third component of spin. Y is isospin.

Gravitation isn't part of Standard Model and it's corresponding boson wasn't found yet. Also there is no quantum field theory of gravitation. Each of the forces can be described by applying a symmetry transformation to a Lagrange density \mathcal{L} and requiring \mathcal{L} to be invariant under this transformation. This process introduces gauge bosons as spin-1 force carriers and coupling constants representing the strength of the force. The transformations are described by symmetry groups and are named after their matrix representation.

The strong force is described by quantum chromodynamics (QCD), which requires \mathcal{L} to be invariant under $SU(3)$ C-transformation. This introduces a strong coupling constant g_s , a strong charge called "color" and eight color-charged massless gluons as mediating gauge bosons. The fact that gluons and quarks carry the strong charge themselves leads to the confinement of strongly-interacting particles: every quark must be in a color-singlet bound state with other quarks, free single quarks or gluons can thus not be observed.

particles	Q	$ \vec{I}^W $	I_3^W	Y	color charge	spin
$\begin{pmatrix} u_L \\ d_L \end{pmatrix}$	$+\frac{2}{3}$	$\frac{1}{2}$	$+\frac{1}{2}$	$+\frac{1}{3}$	r,g,b	$\frac{1}{2}$
$\begin{pmatrix} c_L \\ s_L \end{pmatrix}$	$+\frac{2}{3}$	$\frac{1}{2}$	$-\frac{1}{2}$	$+\frac{1}{3}$	r,g,b	$\frac{1}{2}$
$\begin{pmatrix} \nu_{e,L} \\ e_L \end{pmatrix}$	0	$\frac{1}{2}$	$+\frac{1}{2}$	-1	0	$\frac{1}{2}$
$\begin{pmatrix} \nu_{\mu,L} \\ \mu_L \end{pmatrix}$	0	$\frac{1}{2}$	$-\frac{1}{2}$	-1	0	$\frac{1}{2}$
$\begin{pmatrix} \nu_{\tau,L} \\ \tau_L \end{pmatrix}$	0	$\frac{1}{2}$	$-\frac{1}{2}$	-1	0	$\frac{1}{2}$
u_R	$+\frac{2}{3}$	0	0	$+\frac{4}{3}$	r,g,b	$\frac{1}{2}$
d_R	$-\frac{1}{3}$	0	0	$-\frac{2}{3}$	r,g,b	$\frac{1}{2}$
$\nu_{e,R}$	0	0	0	0	0	$\frac{1}{2}$
e_R	-1	0	0	-2	0	$\frac{1}{2}$
γ	0	0	0	0	0	1
g	0	0	0	0	8 distinct	1
W^+	$+1$	1	$+1$	0	0	1
W^-	-1	1	-1	0	0	1
Z^0	0	1	0	0	0	1
H^0	0	$\frac{1}{2}$	$-\frac{1}{2}$	1	0	0

Figure 1.1: Properties of fermions and gauge bosons.

The electromagnetic force is derived by requiring \mathcal{L} to be invariant under the $U(1)$ - symmetry transformation. This implies a massless chargeless photon as gauge boson. The treatment of the weak interaction is a little more peculiar, as charged weak interactions have been found to be maximal parity violating, whereas neutral weak interactions are not. The charged weak bosons W^\pm only couple to left-handed fermions and right-handed antifermions. These issues are resolved by a theory describing both electromagnetism and weak interaction in an electroweak mixing, which involves $SU(2)_L \otimes U(1)_Y$. This description implies the three-component weak isospin I_W and the weak hypercharge Y as particle properties. The electroweak symmetry is broken to form the electromagnetic interaction with its massless gauge boson γ , and the weak interaction with three massive gauge bosons W^\pm and Z^0 . This symmetry breaking is carried out by the Higgs mechanism and requires an additional scalar Higgs-boson[1,2,3].

1.3 The Feynman calculus and cross section

A quantity of interest in high energy physics scattering experiments is the cross section σ of a particular process. It describes the likelihood of an interaction between particles. The aim is to calculate the total cross section of a physical process from theory and compare it with the experimental measurement. The total cross section of a particular scattering process $1 + 2 + 3 + 4 + \dots + n$ can be calculated using Fermi's Golden Rule:

$$\sigma = \frac{S}{4\sqrt{(p_1 p_2)^2 - (m_1 m_2)^2}} \int \left[|M|^2 (2\pi)^4 \delta^4(p_1 + p_2 + \dots + p_n) \times \prod \left(\frac{1}{2\sqrt{p_j^2 + m_j^2}} \frac{d^3 p_j}{(2\pi)^3} \right) \right]$$

Here, p_j and m_j are the momenta and masses of the involved particles i . S denotes a statistical factor that corrects for double-counting if there are identical particles in the final state. The dynamics of the process is described in its matrix element M , while the kinematic constraints represent the phase space factor ($(2\pi)^4$ and $\delta^4(\dots)$). The calculation of the Matrix element is done in a perturbative way and each step of the expansion can be represented by a so-called Feynman graph. An example is shown in figure 1.2.

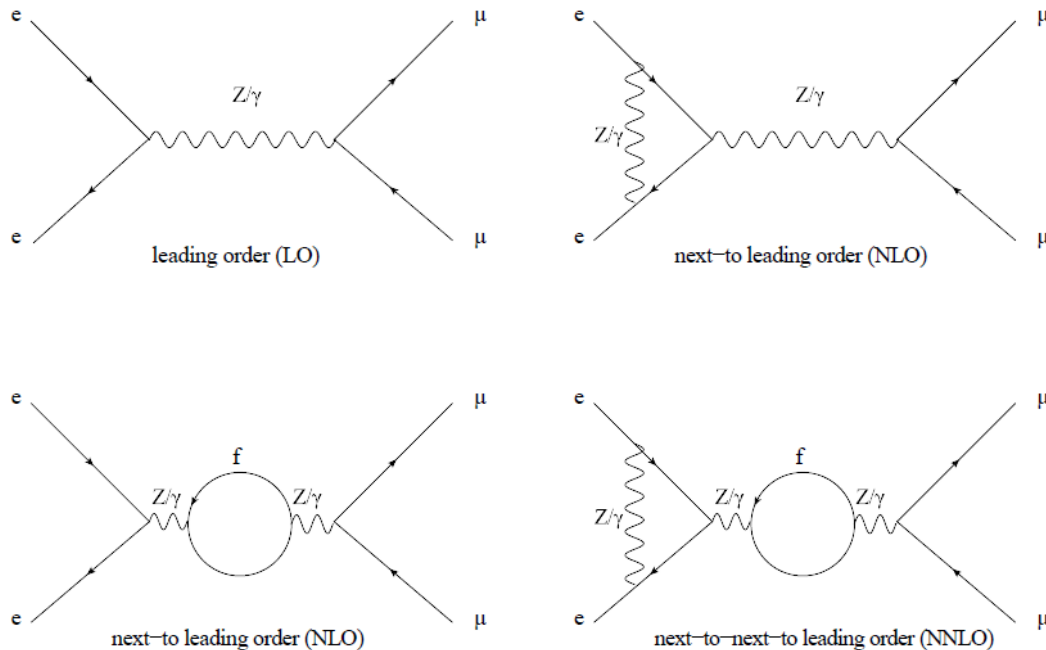


Figure 1.2: Examples of Feynman diagrams[4].

The relation between cross section σ and integrated luminosity L can be used to calculate the expected number of detected events N_{EV} in a particular process:

$$N_{EV} = L \times \sigma \times \epsilon$$

given a detector efficiency ϵ which has to be determined in simulation or data [3]

1.4 CP-Violation

Within the Standard Model the CPT symmetry holds. Idea of this symmetry is that when we have two systems, which behave identically when following properties are inverted:

- opposite charge of particles (particles and in second system antiparticles) – C symmetry
- opposite parity of particles (change of sign of all spatial coordinates for 3 dimensional system) - P symmetry
- opposite time flow – T symmetry

then these two systems will have the same time development. CP symmetry is not conserved in nature in selected processes. It is called CP-Violation and for quark mixing it is well described in the CKM matrix (Cabibbo–Kobayashi–Maskawa matrix). The matrix elements represent probabilities of quark flavor exchange. For example top quark can decay in to bottom quark by weak interaction. This decay is described by matrix elements V_{tb} in the CKM matrix. These matrix elements can be measured in decays of mesons, V_{bc} for example in neutral B meson system (B_0 and \bar{B}_0) decay to final states, when we look at the decay channels of this system with the same final states.

1.5 Muon interaction with detector material

Muons are charged leptons of intermediate mass (see Figure 1.3), so they interact via the weak force, but not via the strong force. Although the muon is not stable, it can travel a long distance before it decays, provided a high momentum implying high Lorentz boost.

lepton flavor	mass (MeV)	mean lifetime	main decay channel(s)
e	0.511	stable	–
μ	105.66	2.197	$e^- \bar{\nu}_e \nu_\mu$
τ	1776.84	$290.6 \times 10^{-15} s$	$\mu^- \bar{\nu}_\mu \nu_\tau$ $e^- \bar{\nu}_e \nu_\tau$ $\pi^- \nu_\tau$ $\pi^- \pi^0 \pi^0 \nu_\tau$ $\pi^- \pi^+ \pi^- \nu_\tau$

Figure 1.3: Properties of the charged leptons.

Muons lose energy in matter due to electromagnetic interaction with material. In principle this includes two different processes:

- bremsstrahlung
- ionization.

The Feynman graphs for these processes are shown in figure 1.4.

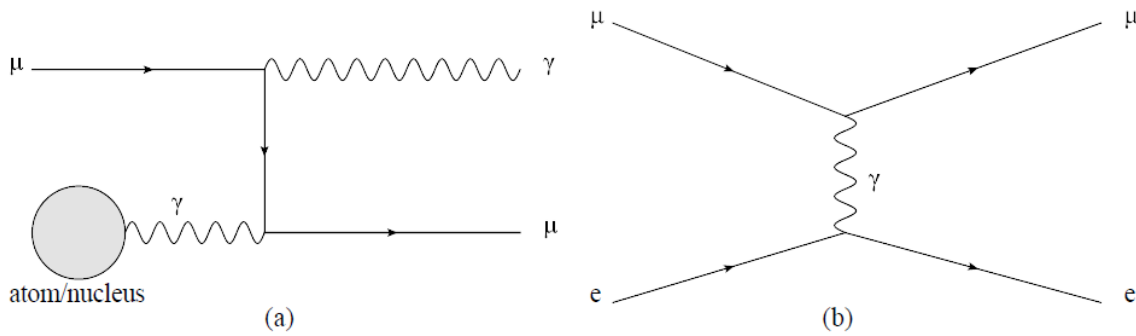


Figure 1.4: Feynman graphs for energy loss through (a) bremsstrahlung and (b) ionization [4].

The amount of energy the muon loses by interactions with the material as it traverses depends on the passed material, the muon's velocity and the traveled distance. For ionization the energy loss per distance can be parametrized by the Bethe-Bloch-Formula:

$$\left(\frac{dE}{dx}\right) = \frac{4\pi\epsilon^4}{c^2 m_e} N_A \frac{Z}{A} z^2 \frac{1}{\beta^2} \left[\frac{1}{2} \ln\left(\frac{2m_e c^2 2\gamma^2 T_m a x}{I^2}\right) - \beta^2 - \frac{\delta}{2} - \frac{C}{Z} \right]$$

The bremsstrahlung energy loss is proportional to the particle energy:

$$\left(\frac{dE}{dx}\right) = \frac{1}{X_0} E$$

X_0 is radiation length, the distance after which the muon has lost 1/e of its initial energy. X_0 depends on the material. The critical energy E_C is an energy for which bremsstrahlung process dominates the energy loss. The critical energy E_C for muons in a solid mater with atomic number Z can be parametrized by the following formula [4]:

$$E_C(\text{GeV}) = \frac{5700\text{GeV}}{(Z + 1.47)^{0.838}}$$

Chapter 2

The Large Hadron Collider and detector ATLAS

2.1 The LHC

The Large Hadron Collider (LHC) is a proton-proton collider that will operate at the highest center-of-mass energies ever achieved, 14 TeV. The LHC accelerator is located at the CERN laboratory near Geneva at the Swiss-French border. Protons are pre-accelerated using a linac to an energy of 50 MeV before being injected in the Proton Synchrotron Booster in which they are accelerated to an energy of 1.4 GeV (see Figure 2.1). The next acceleration step is the Proton Synchrotron (PS) giving the protons an energy of 26 GeV. The Super Proton Synchrotron (SPS) increases the beam energy to 450 GeV which is the energy of the protons when injected to the LHC. The injected protons will reach an ultimate beam energy of 7 TeV in LHC. The LHC is built in the tunnel of the former accelerator, the Large Electron Proton collider (LEP).

The LHC consists of two counter rotating proton beams crossing at four different points along the ring. More than 1200 superconducting dipole magnets with magnetic fields up to 9 T are used to steer the proton beams, consisting of 2808 bunches of protons with 10^{11} protons per bunch. The bunches are inter spaced with a 25 ns time interval, giving rise to 40 million bunch crossings per second at each interaction point. The LHC started up on the 10th of September 2008, successfully sending the proton beams around in the accelerator. A malfunction caused by a faulty electrical connection resulted in mechanical damage on the 19th September of that year. A total of 53 of the superconducting dipole magnets had to be removed from the tunnel for cleaning and repairs. On

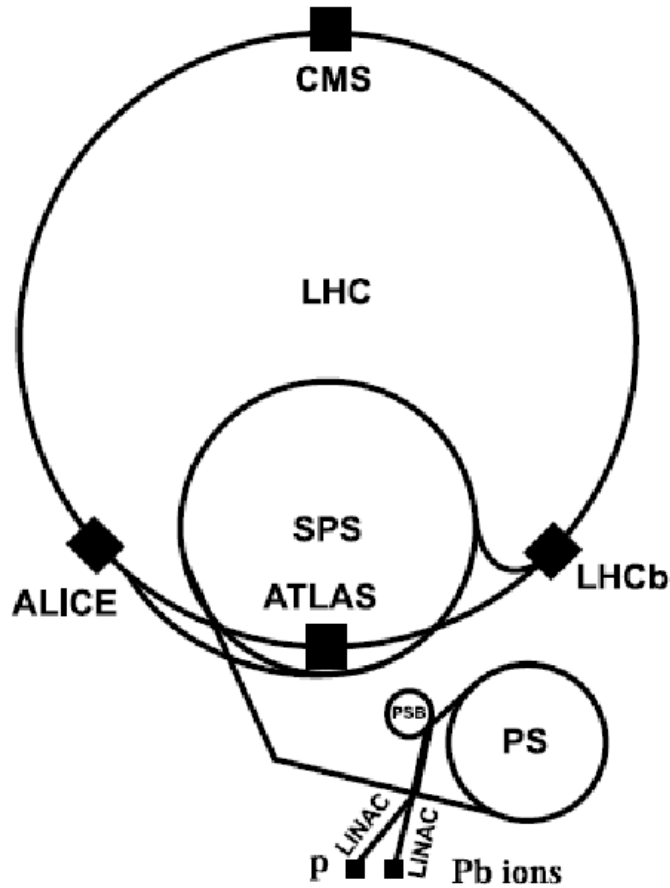


Figure 2.1: The LHC accelerator chain with it's detectors[5].

20 November 2009 the LHC started with circulation of protons again and 3 days later first collisions were recorded. The designed luminosity of $10^{34} \text{ cm}^{-2} \text{ s}^{-2}$ will be reached after a period of operating at a lower luminosity from $10^{28} \text{ cm}^{-2} \text{ s}^{-2}$, plot of the progress is in Figure 2.2. At restart, the LHC ran at a lower center of mass energy of 7 TeV. Four main and two additional detectors are designed and constructed to measure the physics events at the LHC. Two general-purpose detectors, ATLAS and CMS are designed to cover a wide range of physics. The LHCb experiment is dedicated to study B physics and CP violation. ALICE is designed to study physics of the quark-gluon plasma by studying collisions of heavy ions, Pb-Pb collisions at the LHC. TOTEM will measure the total proton-proton cross-section and elastic scattering. LHCf studies the energy distributions of particles very close to the beam line.

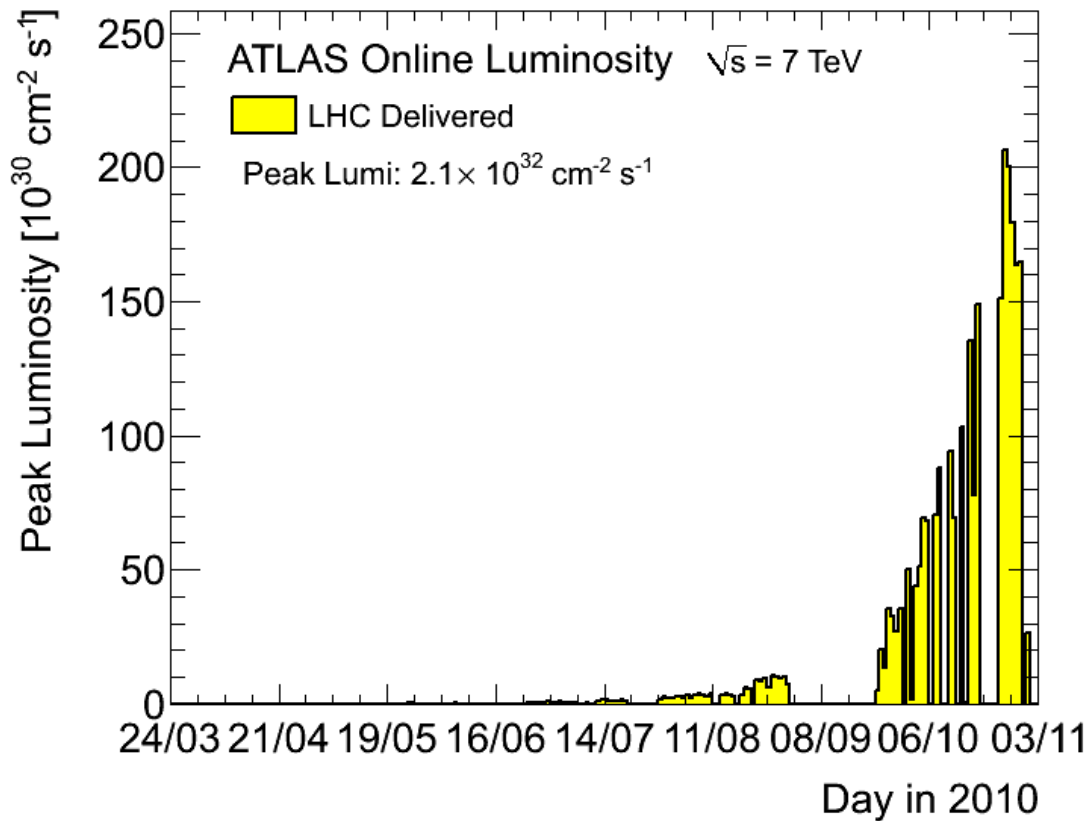


Figure 2.2: Plot of the peak luminosity during year 2010 [5].

2.2 The ATLAS experiment

ATLAS (A Toroidal Lhc ApparatuS) is one of the four large experiments installed at the LHC. One of the main physics issues that the center of mass energy and luminosity of the LHC will allow to investigate is the origin of the spontaneous symmetry-breaking mechanism in the electroweak sector of the Standard Model (SM). This symmetry-breaking is expected produce a SM Higgs boson, or of a family of Higgs particles if the Minimal Super-symmetric Standard Model (MSSM) is considered. The design of the ATLAS detector was therefore optimized to allow the identification of Higgs particles [6].

2.2.1 Overall design

In order to achieve the necessary sensitivity to the physics processes which are to be studied at the LHC, the ATLAS detector was designed to provide:

- Electron and photon identification and measurements, using a very precise electro-

magnetic calorimetry.

- Accurate jet and missing transverse momentum measurements, using, in addition to electromagnetic calorimeters, the full-coverage hadronic calorimetry.
- Efficient tracking and vertexing also at high luminosity, with particular focus on high- p_T lepton momentum measurements.
- Large acceptance in pseudorapidity η , and almost full coverage in ϕ .

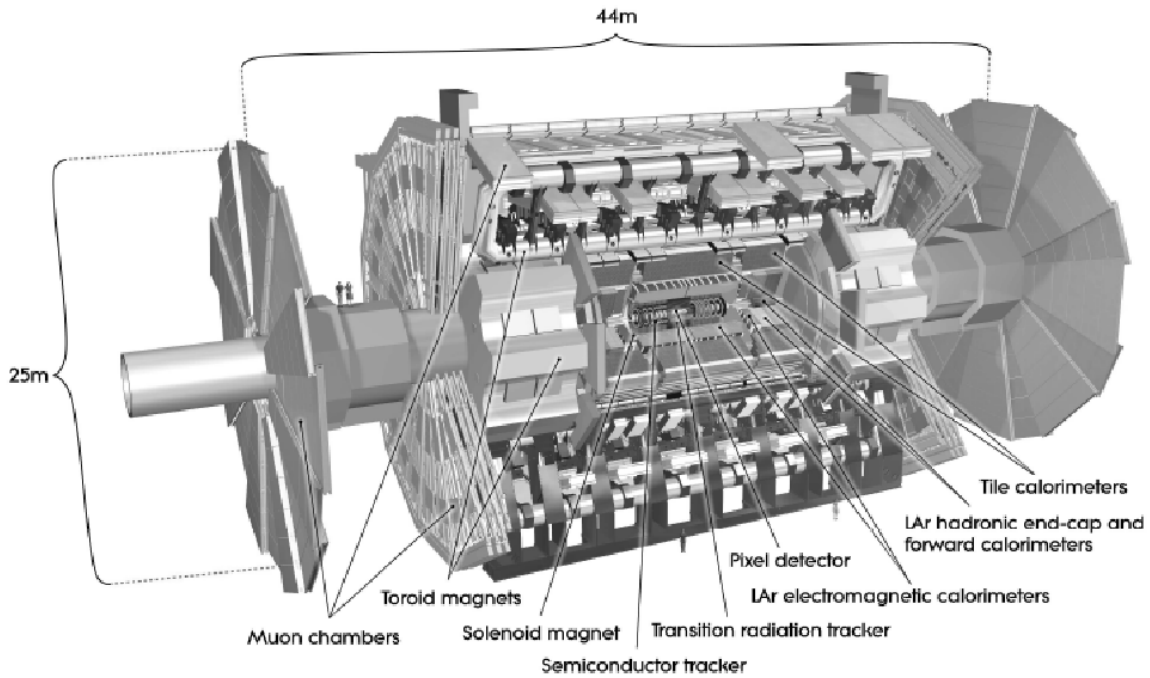


Figure 2.3: The ATLAS detector and its subdetectors [11].

A superconducting solenoid generates the magnetic field in the inner region of the detector, while eight large air-core superconducting toroids are placed outside the calorimetric system, and provide the magnetic field for the external muon spectrometer. ATLAS geometry is shown in Figure 2.3 [11].

2.2.2 The Inner Detector (ID)

The Inner Detector (Figure 2.4.) is entirely contained inside the Central Solenoid, which provides a magnetic field of 2 T. The high track density expected to characterize LHC events calls for a careful design of the inner tracker. In order to achieve the maximum granularity with the minimum of material, it has been chosen to use two different technologies: semiconductor trackers in the region around the vertex are followed by a straw tube tracker.

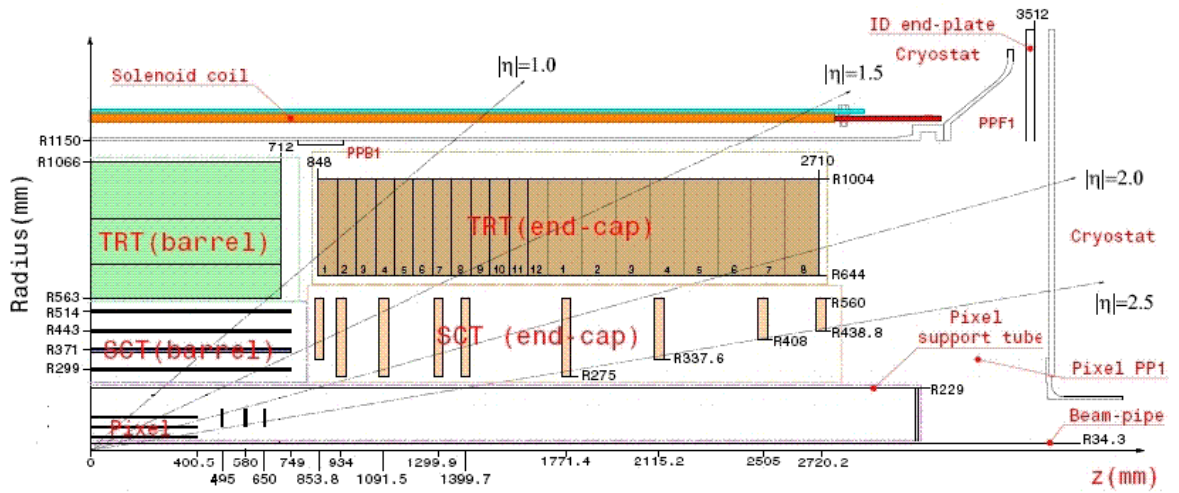


Figure 2.4: Quarter of ATLAS Inner Detector (ID)[6].

2.2.2.1 Pixel Detector

The pixel detector consists of three concentric layers in the barrel and three discs per end-cap in the forward regions. The distances of the three barrel layers to the beam-line are 5.05, 8.85 and 12.25 cm respectively. A traversing charged particle liberates charge in the silicon sensor and a discriminator in the readout electronics determines if the signal is above threshold. The time over threshold value is written out and it allows to reconstruction of the amount of charge that was deposited. The detector contains approximately 80.4 millions of readout channels. Being closest to the interaction point, the pixel detector dominates the impact parameter resolution. Because of its high granularity, the pixel detector plays an important role for pattern recognition as well. The resolution is $12 \mu\text{m}$ in $R\Phi$ and $70 \mu\text{m}$ in z [11].

2.2.2.2 SemiConductor Tracker(SCT)

The Semiconductor Tracker (SCT) is designed to provide four precise measurements per track in the intermediate radial range, contributing to the measurement of momentum, impact parameter and vertex position, as well as providing good pattern recognition by the use of high granularity. The SCT is based upon silicon microstrip detector technology. The detector contains 61 m^2 of silicon detectors, with 6.2 million readout channels. The spatial resolution is $16 \text{ }\mu\text{m}$ in $R\Phi$ and $580 \text{ }\mu\text{m}$ in z [11].

2.2.2.3 Transition Radiation Tracker (TRT)

The straw tubes are parallel to the beam in the barrel while in the endcaps they are placed along the radial direction. Each straw tube has a resolution of $170 \text{ }\mu\text{m}$, and each track crosses about 36 tubes on average. In addition to this, the straw tube tracker can also detect the transition-radiation photons emitted by electrons crossing the xenon-based gas mixture of the tubes, thus improving the ATLAS particle identification capabilities by separating of electrons and pions [11].

2.2.3 The ElectroMagnetic Calorimeter (EM calorimeter)

The EM calorimeter is divided in three parts: barrel ($|\eta| \leq 1.7$) and two end-caps ($1.375 \leq |\eta| \leq 3.2$). The barrel calorimeter is divided in two half barrels, with a small (6mm) gap between them at $z = 0$. Each end-cap calorimeter is made up of two coaxial wheels. The EM calorimeter is a Liquid Argon detector with lead absorber plates and Kapton electrodes. In order to provide a full coverage in η an accordion geometry was chosen for the internal layout of the calorimeter. The lead absorber layers have variable thickness as a function of η and has been optimized to obtain the best energy resolution. On the other hand, the LAr gap has a constant thickness of 2.1 mm in the barrel. The total thickness is $\geq 24X_0$ in the barrel and $\geq 26X_0$ in the end-caps.

In the region with $\eta \leq 2.5$ the EM calorimeter is longitudinally divided in three sections. The first region is meant to work as a preshower detector providing particle identification capabilities and precise measurement in η . It has a thickness of $6 X_0$ constant as a function of η , is read out with strips of 4mm in the η direction [11].

2.2.4 The Hadronic Calorimeter

The region with $|\eta| \leq 4.9$ is covered by the hadronic calorimeters using different techniques, taking into account the varying requirements and radiation environment over this large range. The range $|\eta| \leq 1.7$, corresponding to the barrel calorimeter, is equipped with a calorimeter (TileCal) based on the iron/scintillating tile technology. Over the range $1.5 \leq |\eta| \leq 4.9$, Liquid Argon calorimeters were chosen. In this region the hadronic calorimetry is segmented into an Hadronic End-Cap Calorimeter (HEC), extending up to $|\eta| \leq 3.2$ and a High Density Forward Calorimeter (FCAL) covering the region with highest η . Both the HEC and the FCAL are integrated in the same cryostat housing the EM end-caps calorimetry. The thickness of the calorimeter has been carefully tuned in order to provide good containment of hadronic showers and reduce to minimum the punch through into the muon system. At $\eta = 0$ the total thickness is 11 hadronic interaction lengths, including the contribution from the outer support. This has been shown by measurements and simulations to be sufficient to reduce the punch through to just prompt or decay muons and 10 layers of active calorimeter provide good resolution for high energy jets. This characteristics, together with the large coverage, will guarantee an accurate E_{miss} measurement, which is an important parameter in the signatures of many physics processes [11].

2.2.5 The Magnet system

ATLAS is characterized by two different magnetic field systems required for particle identification and momentum measurements: **Central Solenoid** (CS) is a super-conducting solenoid providing a magnetic field of 2 T; it is installed around the Inner Detector cavity with a radius of 1.2 m and a length of 5.3 m. It is optimized to minimize the amount of material in front of the electromagnetic calorimeter. The large super-conducting air-core toroid system is constituted by eight Barrel Toroids (BT) and two End-Cap Toroids (ECT) (see Figure 2.5), with an open structure to minimize the contribution of multiple scattering to the momentum resolution. Over the range $\eta \leq 1$, magnetic bending is provided by the large barrel toroid, extending over a length of 25 m, with an inner core of 9.4 m and an outer diameter of 20.1 m. For $1.4 \leq |\eta| \leq 2.7$, charged tracks are bent by the two end-cap magnets inserted into both ends of the barrel toroid. They have a length of 5 m, an inner core of 1.64 m and an outer diameter of 10.7 m. For range $1 \leq |\eta| \leq 1.4$ (usually called transition region) magnetic detection is provided by a combination of

barrel and end-cap. This magnets configuration provides a strong magnetic field, that is mostly orthogonal to the muon trajectories and it has maximum value ≈ 4 T [7].

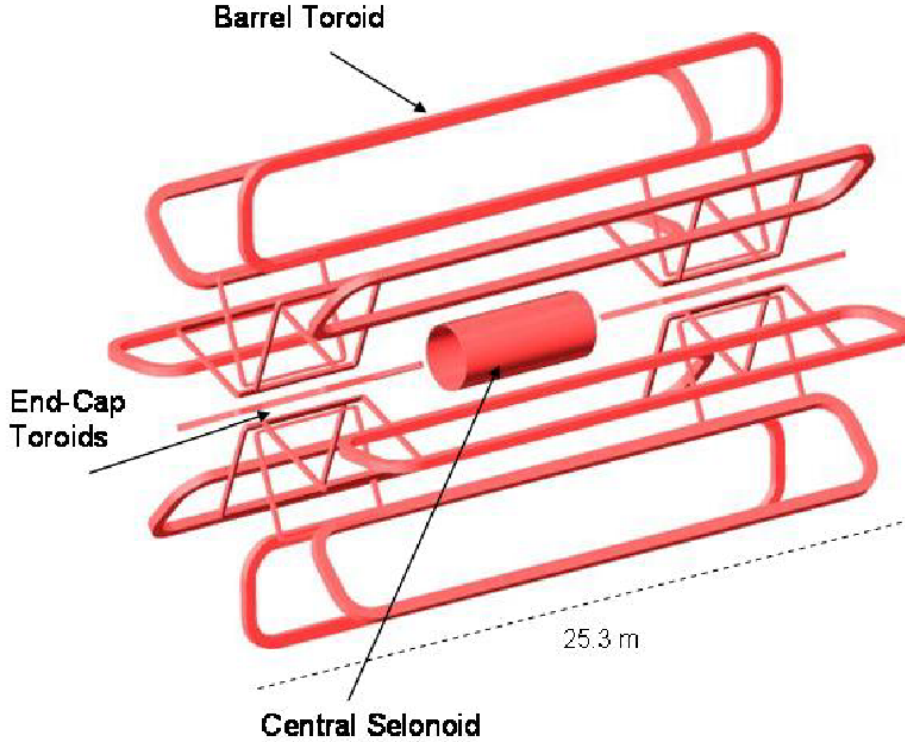


Figure 2.5: The ATLAS magnet system [7].

2.2.6 The Muon Spectrometer

The main feature of the ATLAS experiment is the design of the Muon Spectrometer which uses a toroidal magnetic field. Muon spectrometer has two functions: trigger and precision measurement of tracks. This is why muon spectrometer contains two separate systems with distinct functionality:

- Trigger

The muon trigger system is made of two types of chambers depending on region. In barrel region there are used Resistive Plate Chambers (RPCs) and the end-caps triggering chambers are made from Thin Gap Chambers (TGCs). This system of chambers covers the range up to $|\eta| = 2.4$. This types of chambers generates fast signal with time resolution in order of nanoseconds with track resolution is about 1 cm.

- Precision measurement

This part of muon spectrometer is also made of two types of chambers. In most η -range we used Monitored Drift Tube (MDTs) and for large η and in closeness to interaction point was used Cathode Strip Chambers (CSCs).

2.2.6.1 Monitored Drift Tube Chambers (MDTs)

The Monitored Drift Tube Chambers perform the precision coordinate measurement in the bending direction of the toroidal magnet and therefore provide the muon momentum measurement. The basic detection elements of the MDTs chambers are aluminum tubes of 30 mm diameter and 400 μm wall thickness, with a 50 μm diameter central W-Re wire. The tubes are operated with a non-flammable gas mixture at 3 bar absolute pressure. The wire is held in place by a plug at each end of the tube. The wire is the anode with a potential of 3270 V. The amplification factor of the gas is very low, only 2×10^4 to minimize aging effects. In the MDTs the drift time of the ionized electrons is measured, since the maximum drift time is about 700 nsec, the MDTs are not suited for trigger measurements. As known, linear relation between the drift time to the drift distance allows a single-wire resolution of 80 μm . In Figure 2.7, we can see the geometry of MDTs modules [8].

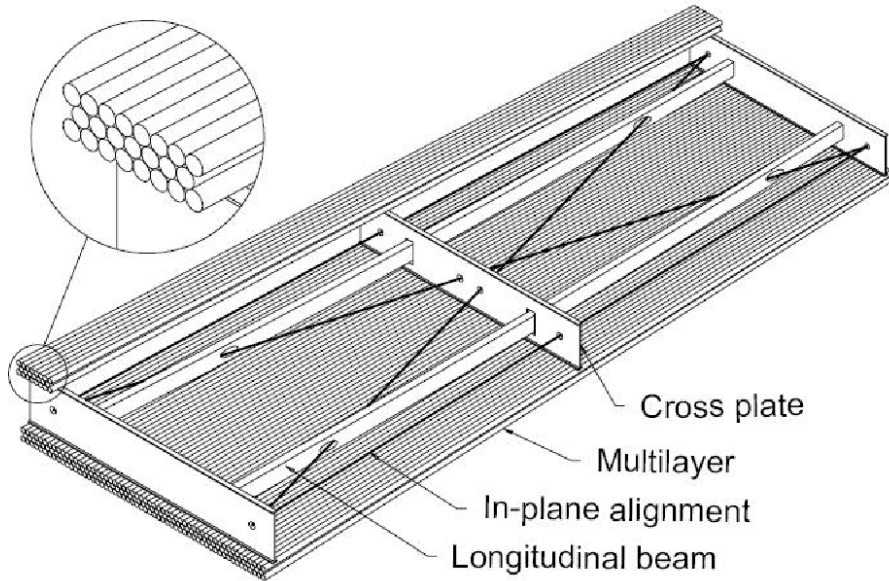


Figure 2.6: Design of ATLAS MDTs modules[8].

2.2.6.2 Cathode Strip Chambers (CSCs)

The Cathode Strip Chambers (CSCs) are used for precision measurements in areas where high background rates exist. This areas give first muon measurement of position at pseudorapidities $|\eta| \geq 2.0$. These chambers have good measurement resolution of $80 \mu\text{m}$. The CSCs are multi-wire proportional chambers [Figure 2.8] with symmetric cells in which anode-cathode spacing d is equal to space between anode wires, which has been fixed at 2.54 mm. The cathode readout pitch is 5.08 mm. The CSCs are arranger in 2×4 layers. They are mounted in such a way as to provide an eight-layer measurement in two groups of layers, gap between them is 90 mm. The CSCs operate with a non-flammable hydrogen free gas mixture. This combination of gas and small gap width has low sensitivity to neutron backgrounds. The maximum drift time is about 30 ns.

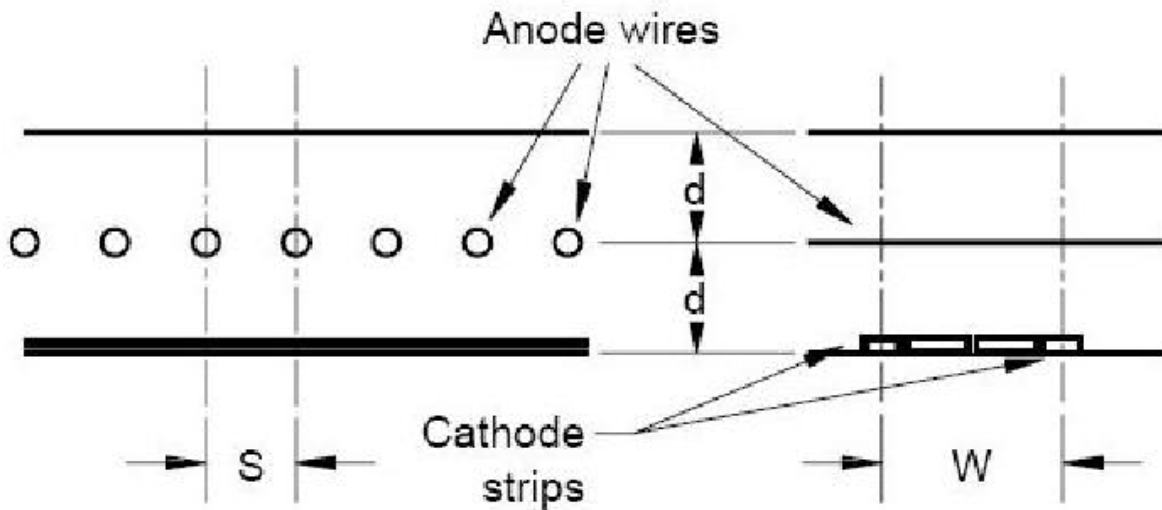


Figure 2.7: Schematic diagram of Cathode Strip Chambers [12].

2.2.6.3 Resistive Plate Chambers (RPCs)

The RPCs are located in the barrel and divided into three stations, each with two detector layers. Two stations installed at a distance of 50 cm from each other are located near the center of the magnetic field region, while the third station at the outer radius of the magnet. The basic RPC unit is a narrow gas gap formed by two parallel resistive bakelite plates, separated by insulating space. Between the plates there exist a uniform electric field of few kV/mm. This field multiplies the ionization electrons into an avalanche producing a typical pulse of 0.5 pC. The signal is read out via capacitive coupling by metal

strips on both sides of the detector. The RPC provides a typical spacetime resolution of $1 \text{ cm} \times 1 \text{ nsec}$. The RPC is made from two rectangular detector layers, each one read out by two orthogonal series of pick-up strips. The strips parallel to the MDT wires provide the bending view of the trigger detector. The strips orthogonal to the MDT wires provide the second-coordinate measurement. The 2 mm thick bakelite plates are separated by polycarbonate. The outside surfaces of the resistive plates are coated with thin layers of graphite paint which are connected to the high voltage supply. These graphite electrodes are separated from the pick-up strips by $200 \mu\text{m}$ thick insulating films which are glued on both graphite layers. Each chamber is made from two detector layers and four readout strip panels. These elements are rigidly held together by two support panels [8].

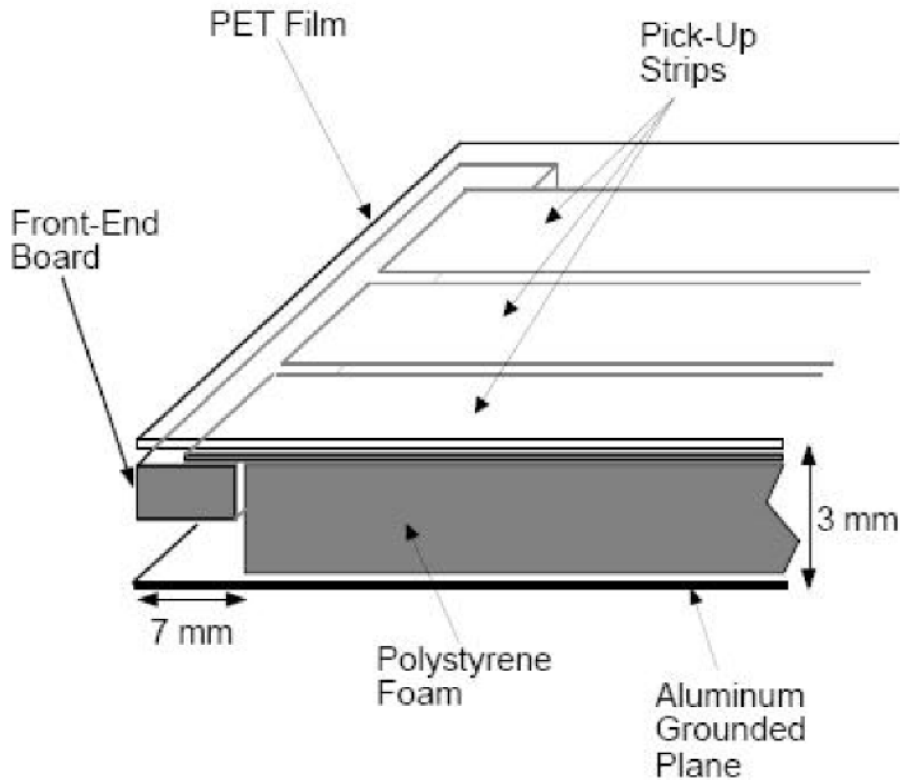


Figure 2.8: Layout of RPC read-out [8].

2.2.6.4 Thin Gap Chambers (TGCs)

The Thin Gap Chambers provide two functions in the end-cap of the ATLAS Muon Spectrometer: the muon trigger capabilities and the azimuthal coordinate to complement the bending coordinate measured by the MDTs. TGCs are multi-wire proportional chambers.

Their structure is similar to the CSCs, except that the anode-to-anode distance (1.8mm) is larger than the cathode-to-anode distance (1.4mm).

Similar to RPCs, the TGCs measure two coordinates. A TGC is built from wires which are arranged parallel to the MDT wires and from strips arranged orthogonally to the wires. Signals from the anode and the strips provide the trigger information. The readout strips are also used to measure the second coordinate. As trigger chambers, the TGCs are required to have good time resolution to provide bunch-crossing identification. The TGC operates in saturated mode at high voltage of 3.1 kV. The saturated mode has the advantage of small sensitivity to mechanical deformations and small dependence on the incident angle. The TGC's electric field configuration and the small wire distance provide a short drift time. Reading all wires provides higher momentum resolution than needed. To match the geometric granularity to the needed momentum resolution it is sufficient to group several wires together. The number of wires in a wire-group varies, as function of η , from 4 to 20 wires [8].

Chapter 3

Trigger

One of the main challenges at the LHC is the trigger system. The search for new physics requires unprecedented rate of 10^9 interactions per second, for enough statistics. By practical limitations of the off-line computing power and storage capacity, the ATLAS event storage rate is limited to approximately 100 Hz (average size of 1 MB per event). Therefore an overall 10^7 rejection factor against minimum-bias processes while retaining excellent efficiency for the rare new physics, such as Higgs boson decays.

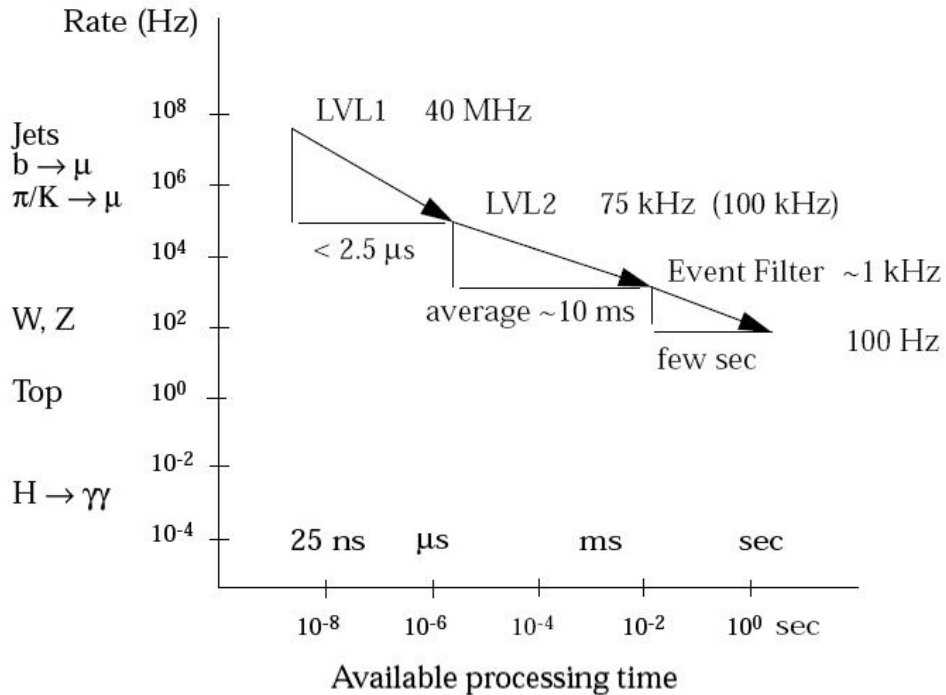


Figure 3.1: Event rate and decision stages [12].

The ATLAS trigger and data-acquisition system is based on three levels of on-line event selection, see Figure 3.2. Each trigger level refines the decisions made at the previous level and, where necessary, applies additional selection criteria. The ATLAS initial bunch-crossing rate is 40 MHz. At high luminosity, each bunch crossing contains about 23 interactions (interaction rate 10^9 Hz at a luminosity of 10^{34} cm⁻² sec⁻¹). The three trigger levels of the ATLAS detector are: LVL1 (level-1), LVL2 (level-2) and Event Filter (EF). When we talk about LVL2 and EF trigger we call them High level trigger (HLT). The LVL1 trigger receives data at the full LHC bunch-crossing rate of 40 MHz. The output rate is limited by the capabilities of the front-end systems to 75 kHz (upgradeable to 100 kHz). LVL2 will reduce rate of events by two orders of magnitude, resulting in 1kHz input rate into the Event Filter. The final reduction will be done in the Event Filter to a final rate of about 100-200 Hz. This rates and available processing time are given in Figure 3.1.

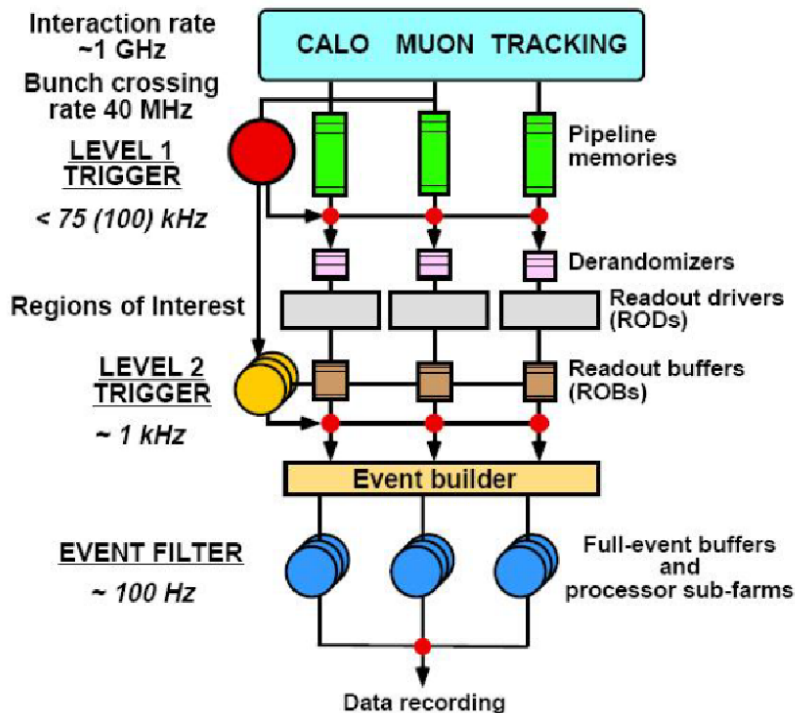


Figure 3.2: Block diagram of trigger system [11].

3.1 Level 1 trigger (LVL1)

The Level 1 trigger system receives data at the full LHC bunch crossing rate of 40 MHz and must make its decision within $2.5 \mu\text{s}$ to reduce the output rate to 75 kHz (40 kHz during ATLAS start-up). The L1 trigger has dedicated access to data from the calorimeter and muon detectors. The LVL1 calorimeter trigger decision is based on the multiplicities and energy thresholds of the following objects observed in the ATLAS Liquid Argon and Tile calorimeter sub-system: Electromagnetic (EM) clusters, taus, jets, missing transverse energy $E_{T\text{miss}}$, scalar sum E_T in calorimeter, and total transverse energy of observed LVL1 jets. These objects are computed by the LVL1 algorithms using the measured E_T values in trigger towers of 0.1×0.1 granularity in $\Delta\eta \times \Delta\psi$. The LVL1 muon trigger uses measurement of trajectories in the different stations of the muon trigger detectors: the Resistive Plate Chambers (RPC) in the barrel region and the Thin Gap Chambers (TGC) in the endcap region. The input to the trigger decision is the multiplicity for various muon p_T thresholds. There is a limited number of configuration choices that are available at LVL1. The most common difference between configuration choices is the amount of transverse energy or momentum required, so we refer to these configurations as “thresholds”, but note that in addition to the E_T threshold condition, three different isolation criteria can be applied for LVL1 EM and tau objects, and three different window sizes can be specified for LVL1 jet objects. Table 3.1 gives the number of these so-called thresholds that can be set for each object type. The total number of thresholds allowed for EM and tau objects is 16, where 8 are dedicated to be EM objects and 8 can be configured to be either EM or tau objects. The forward jets have four thresholds that can be set independently in each of the detector arms.

Object	EM	Taus	Jets	For. Jets	E_{miss}	$\sum E_T$	$\sum E_T$ (Jets)	$\mu \leq 10\text{GeV}$	$\mu \geq 10\text{GeV}$
# of thresholds	8 - 16	0 - 8	8	4 + 4	8	4	4	3	3

Table 3.1: Number of L1 thresholds that can be set for each LVL1 object type at any given time [6].

The total number of allowed LVL1 configurations (also called LVL1 items) that can be deployed at any time is 256. Each of these LVL1 items, programmed in the Central Trigger Processor (CTP), is a logical combination of the specified multiplicities of one or more of the configured LVL1 thresholds. As an example L1_EM25i and L1_EM25 (A single LVL1 EM object with $E_T \geq 25$ GeV with and without isolation respectively) uses two LVL1 EM thresholds while L1_2EM25i (Two L1 isolated EM object with $E_T \geq 25$ GeV) uses the same LVL1 threshold as the L1_EM25i item. Furthermore, for each of the 256 LVL1 items, a prescale factor N can be specified (where only 1 in N events is selected

and passed to the HLT for further consideration). As the peak luminosity drops during a fill, the LVL1 prescale value can be adjusted to keep the output bandwidth saturated without stopping and restarting a data-taking run, if desired [6,9,11,13].

3.2 Level 2 trigger (LVL2)

The LVL2 trigger is software-based, with the selection algorithms running on a farm of commodity PCs. The selection is largely based on regions-of-interest (RoI) identified at LVL1 and uses fine-grained data from the detector for a local analysis of the LVL1 candidate. A seed is constructed for each trigger accepted by LVL1 that consists of a p_T threshold and an $\eta - \phi$ position. The LVL2 algorithms use this seed to construct an RoI window around the seed position. The size of the RoI window is determined by the LVL2 algorithms depending on the type of triggered object (for example, a smaller RoI is used for electron triggers than for jet triggers). The LVL2 algorithms then use the RoI to selectively access, unpack and analyse the associated detector data for that $\eta - \phi$ position. The ability to move, unpack, and analyse the local data only around the seed position greatly reduces both the processing times and the required data bandwidth. The LVL2 algorithms provide a refined analysis of the LVL1 features based on fine-grained detector data and more optimal calibrations to provide results with improved resolution. They provide the ability to use detector information that is not available at LVL1, most notably reconstructed tracks from the Inner Detector. The information from individual sub-systems can then be matched to provide additional rejection and higher purity at LVL2. For each LVL1 RoI, a sequence of LVL2 algorithms is executed which compute event feature quantities associated with the RoI. Subsequently, a coherent set of selection criteria is applied on the derived features to determine if the candidate object should be retained. The LVL2 farm will consist of around 500 quad-core CPUs. On average, the LVL2 can initiate the processing of a new event every 10 μ s. The average processing time available for LVL2 algorithms is 40 ms, which includes the time for data transfers. The LVL2 system must provide an additional rejection compared to LVL1 of about 40 to reduce the output rate down from 75 (40) kHz to 2 (1) kHz during nominal (startup) operations [6,9,11].

3.3 Event Filter (EF)

The final on-line selection is performed by software algorithms running on the Event Filter (EF), a farm of processors that will consist of 1800 dual quad-core CPUs. The EF receives events accepted by LVL2 at a rate of 2 kHz (1 kHz) during nominal (startup) operations and must provide the additional rejection to reduce the output rate to 200 Hz, corresponding to about 300 MB/s. An average processing time of 4 μ s per event is available to achieve this rejection. The output rate from the Event Filter is limited by the off-line computing budget and storage capacity.

As in LVL2, the EF works in a seeded mode, although it has direct access to the complete data for a given event as the EF selection is performed after the event building step. Each LVL2 trigger that has been accepted can be used to seed a sequence of EF algorithms that provide a more refined and complete analysis. Unlike LVL2, which uses specialized algorithms optimized for timing performance, the EF typically uses the same algorithms as the off-line reconstruction. The use of the more complex pattern recognition algorithms and calibration developed for offline helps in providing the additional rejection needed at the EF [6,9,11].

3.4 Muon triggers

3.4.1 Level-1 muon trigger

The muon trigger receives as input the pattern of hit strips (and wire groups in the case of the TGC detectors) in the muon Trigger chambers. The trigger searches for patterns of hits consistent with high- p_T muons originating from the interaction region. The logic provides six independently-programmable p_T thresholds. The output sent to the Central Trigger Processor (CTP) for each bunch-crossing is the multiplicity of muons for each of the six p_T thresholds. As indicated in Figure 3.3, the muon trigger system is subdivided into a part specific to the RPC chambers, a part specific to the TGC chambers, and a part that combines information from the full system and prepares the input to the CTP. Since the muon trigger decision needs to be very fast, the p_T of the muons is not calculated exactly, but estimated using coincidence maps. In each region of the LVL1 muon trigger (the barrel and the end-cap) one of the three planes is a 'pivot plane' (RPC2 in the Barrel region and TGC3 in the EndCap region). All of the LVL1 algorithms are done

in reference to this plane, see Figure 3.4. A straight line from the hit point in the pivot plane to the interaction point, corresponds to straight tracks fired from the interaction point with infinite momentum. Since the muons do not have infinite momentum and there is a magnetic field in the detector; the muons tracks are bent. Therefore each pivot pixel is associated to a coincidence window, in the low and the high p_T planes [13].

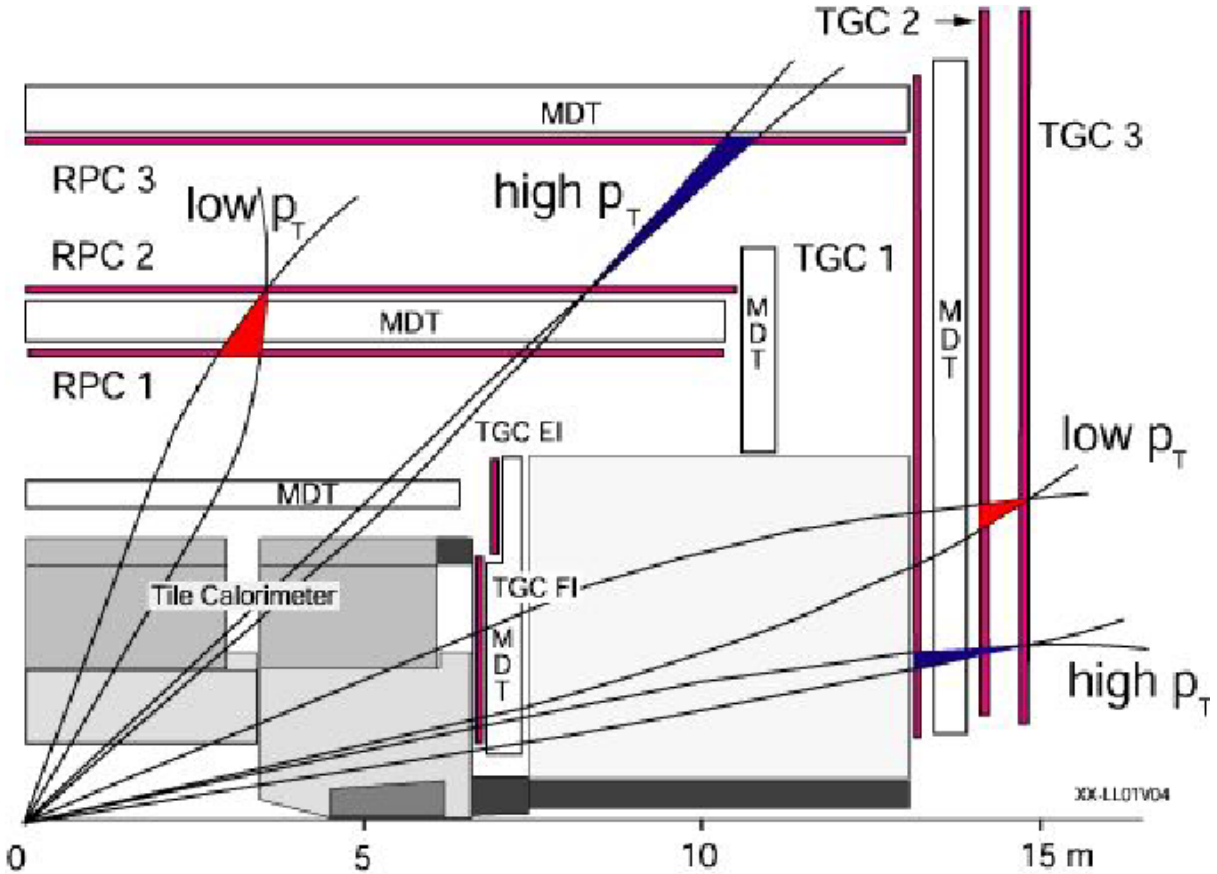


Figure 3.3: Longitudinal view of the end-cap and barrel muon spectrometer with colored systems used by LVL1 trigger [8].

The role of the window is to determine if the inputs are compatible with a muon track. To be compatible with a track of a given momentum an input pixel should fit in the coincidence window around the coincidence infinite momentum pixel. The width of the window around the diagonal depends on the required transverse momentum threshold. The window extends on both sides of the diagonal corresponding to both positive and negative charged muons. Each coincidence matrix operates with three programmable thresholds for the low p_T coincides and three for high p_T . As for now, these thresholds correspond to 6, 8, 10 GeV/c, for the low p_T . The high p_T thresholds are 11, 20,

40 GeV/c. The lower the p_T threshold the wider the coincidence window. The width of the coincidence window depends on the p_T threshold, the coordinate and the muon spectrometer layout. Hence different areas of the detector will have a different set of coincidence maps (one for each p_T threshold) [12,13].

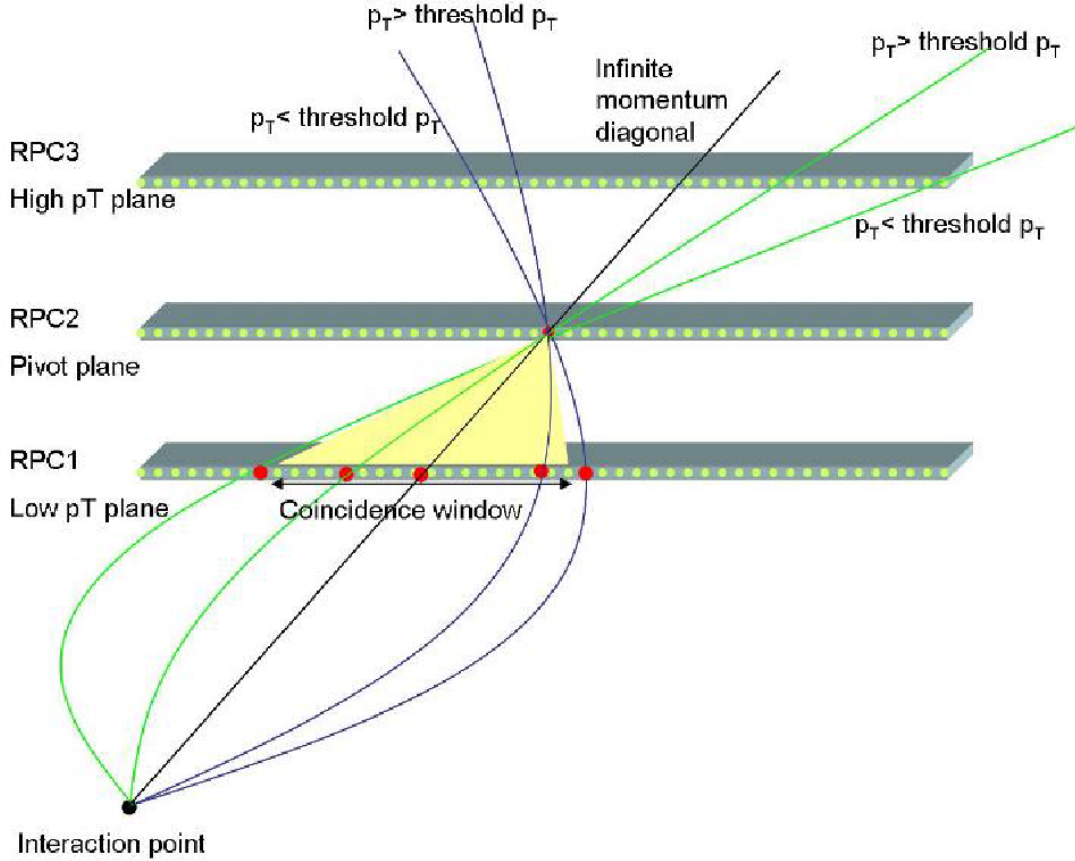


Figure 3.4: System of thresholds based on pivot plane interaction [12].

3.4.2 Level-2 muon trigger

In ATLAS the event selection is performed in three sequential levels of increasing complexity. The Level-1 is implemented with custom hardware and uses low granularity data from a subset of the trigger detectors to identify physics objects within Regions of Interests (RoIs). It reduces the input event rate of 40 MHz to 75 KHz. The higher trigger levels provide a software based event selection which further reduces the event rate to

about 100 Hz. The Level-2 uses the full granularity data, but examines only the RoIs to confirm the physics objects flagged by the Level-1 and to perform a first event selection via physics menus. At this stage the event data are stored in several buffer memories (Read Out Buffers, ROBs), and only those requested by the algorithms are sent to the trigger processor. After the Level-2 selection, the Event Filter (Level-3) takes the final decision using the full event data. The Level-2 Muon trigger task is to confirm muons found at Level-1 by means of a more precise muon momentum measurement (*muon feature extraction*) and to reject fake Level-1 triggers induced by physics background. The better quality of momentum measurement allows for a sharper p_T threshold, but the trigger system requires to exploit the full potential of the ATLAS Muon Spectrometer within 10 ms imposed by the overall latency of the Level-2 trigger system. Thus not only a fast feature extraction algorithm has to be employed, but also a fast access to the data is needed since the data to be processed come from different parts of the Muon Spectrometer. This latter is achieved organizing the data flow in such a way to minimize the traffic towards the trigger processors and using an appropriate format which allows a fast data decoding. Finally the method employed for feature extraction has to be as simple as possible to save processing time. It is the result of an optimization between the CPU usage and the physics performance needed to trigger interesting events: high selection efficiency for high- p_T muons and high rejection of low- p_T muons[12].

3.4.2.1 MuFast algorithm

The Level-2 feature extraction algorithm MuFast, performs the muon track reconstruction in the Spectrometer and measures the transverse momentum of the muon at the interaction vertex. It is steered by the level-1 RoI data consisting of the p_T threshold fired at Level-1 and the position of the RoI. This latter identifies the ROB that stores detector data from a trigger tower. The algorithm requests two ROBs for each RoI, corresponding to the trigger towers containing the Level-1 RoI and the closest one respect to the exact RoI position. This allows the processing of muons passing through two trigger towers. MuFast processes the collected data in three sequential steps: *pattern recognition* involving trigger chamber hits and the position of the MDT hit tubes, *track fit* performed on each MDT chamber, and *p_T estimate* using Look up Tables (LUTs) in order to avoid time consuming fitting methods. The track position at the entrance of the Spectrometer, the direction of flight and the p_T at the interaction vertex are the computed muon features [10].

3.4.2.1.1 Pattern recognition The pattern recognition is designed to select clusters of MDT tubes belonging to a muon track without using the drift time measurement. Being seeded by the RPC trigger data, *muon roads* are opened in each MDT chamber and hit tubes are collected according to the position of the sensitive wire. No track fit is performed at this stage, because solving all combination of different hits would take too much of computing time. The starting point of the pattern recognition is an algorithm that emulates the Level-1 trigger to find the RPC hits that fired the Level-1 trigger (trigger pattern). Those hits are used to compute the initial muon trajectory. The nominal vertex position is used for defining the trajectory of both low- p_T and high- p_T candidates because it increases the accuracy of the muon path extrapolation over areas, where RPC hits are not available. Subsequently, the MDT hit finding procedure is started opening muon roads around the resulting Level-1 trajectory. For each hit tube the residual from the initial trajectory is computed and the tube position is stored if its residual is inside the road (Figure 3.5).

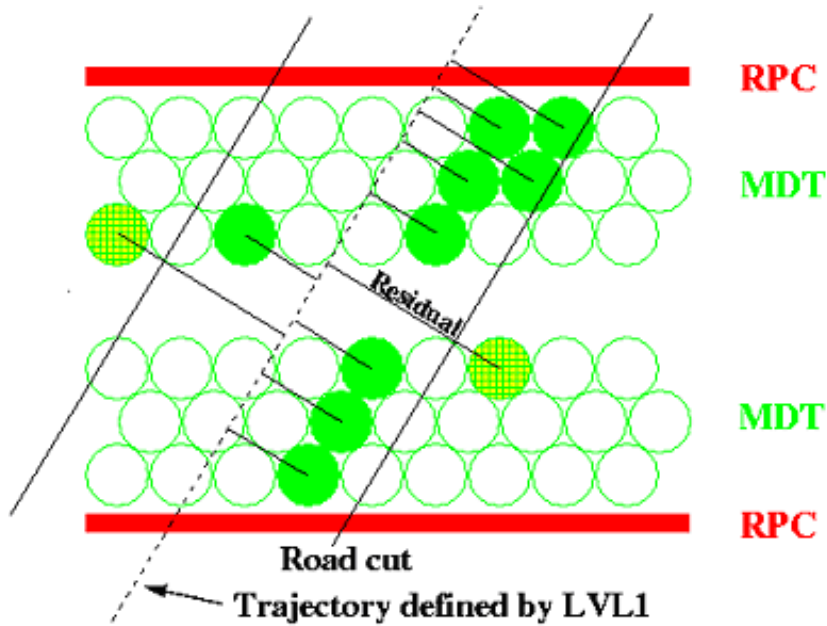


Figure 3.5: Finding of muon trajectory based on LVL1 RoI[10].

The road width is tuned to collect 0.96 of muon hits, it is computed for both low- p_T and high- p_T candidates and for each muon sector (Large, Small and Special). This allows to optimize the road cut for different muon paths and magnetic field values. Finally a contiguity algorithm is applied on the selected hits in order to remove the background. This is a recursive procedure in which the mean position of the track cluster is computed

and the hit tube having the highest deviation from the mean is removed. The contiguity algorithm terminates only when a single hit tube on each MDT layer is left. All together the muon hit selection has 0.96 of efficiency with small background contamination.

3.4.2.1.2 Track fit The track reconstruction approximates the muon track with straight segments obtained separately on each MDT chamber. The advantage of this approach is that, whilst a complete helix fit through the spectrometer would require a time consuming minimization procedure, a linear fit has an analytic solution and doesn't need the magnetic field map. Nevertheless the momentum reconstruction is not significantly degraded by this approximation: the sagitta of a 6 GeV p_T muon within a chamber is typically 500 μm , while it spans from 20 cm to 30 cm within the spectrometer. Using the drift time measurement, a track segment is built if at least four MDT hits (two per MDT multilayer) can be used for the fit (figure 3.6). The left-right ambiguity with respect to the sensitive wire is solved computing all the possible combinations of segments and choosing the one with the best χ^2 . The fit segment provides a precision measurement (super point) of the muon track to measure the bending of the muon in the spectrometer. Fakes from Level-1 are rejected requiring at least two super point in the event. No cut is applied on the quality of the fit because this introduces inefficiency in the selection: due to the straight line approximation, the fit quality is not good either in case of a real muon track.

To achieve good physics performance, the effective time-distance relationship of the MDT tubes is employed. Thus the MDT calibration constants are accessed run-time for converting the drift time into a space measurement and for subtracting the time-of-flight and the propagation time along the sensitive wire. This latter requires the measurement of the muon track in the r - ϕ view which is provided by the RPC data.

3.4.2.1.3 p_T estimate In the present implementation of the algorithm the track bending is measured through the sagitta (s_m), that is computed from three super points as shown in figure 3.7. An estimate of the muon p_T is then found using the inverse linear relationship between the sagitta and the p_T

$$\frac{1}{s_m} = A_0 p_T + A_1$$

This formula is valid for tracks originating at the nominal interaction point. The A_0 parameter is related to the setup of the spectrometer (magnetic field, lever arm) while the A_1 parameter takes into account the energy loss in the calorimeter. This function

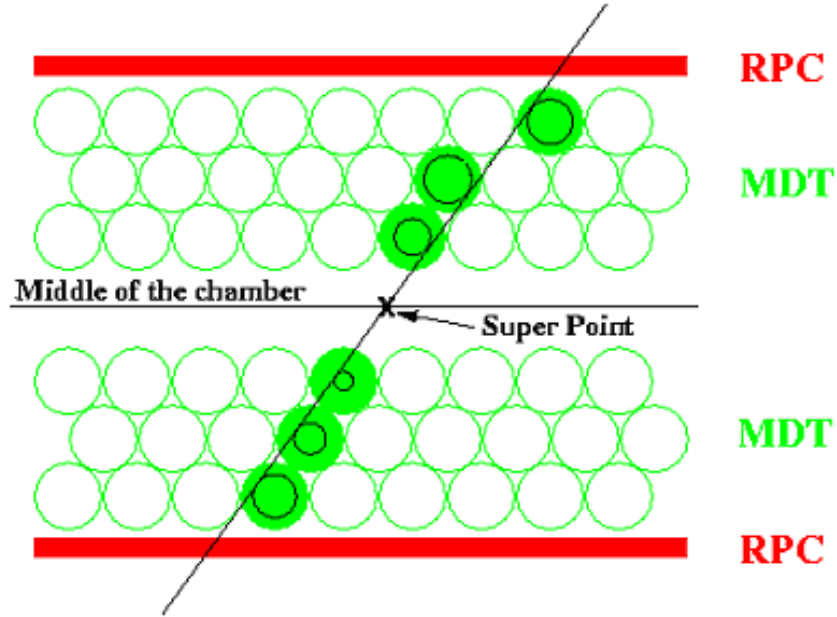


Figure 3.6: The track fit uses the drift time measurements (represented as a circle inside the tubes) to fit the best straight line crossing all the hit tubes. The fit output is the track super point[10].

has been mapped into a Look-up Table by dividing the detector region in which the algorithm operates into η and ϕ bins and computing the A0 and A1 parameters for each bin. This allows a very fast estimation of the muon p_T from the track sagitta anywhere in the region of the LUT calculation. The muon track is assigned to a given η - ϕ cells according to its position at the entrance of the spectrometer.

The multiple scattering at the external surface of the calorimeter, the energy loss fluctuations and the non uniformity of the magnetic field are the main sources of the uncertainty on the p_T estimation and depend on the muon path through the apparatus. Thus the LUT binning has to be optimized to minimize these contributions; a binning of 30 cells in ϕ and 60 cells in η has been seen to be adequate to calibrate the muon reconstruction inside a physics sector of the spectrometer. The finite size of the LUT is rendered less important through the use of an interpolation procedure.

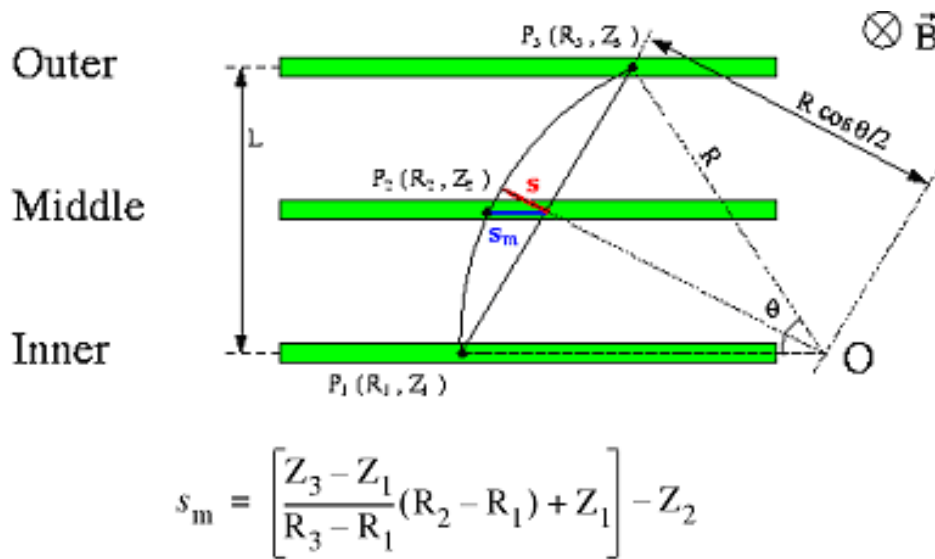


Figure 3.7: The track bending (p_T estimate) is computed with a sagitta (s_m) method. Three points are required to compute s_m : P_1, P_2 and P_3 as illustrated in the figure[10].

Chapter 4

Data analysis

4.1 Data samples

For this work an analysis of two different types of collision data was performed. For measurement of efficiency of the LVL1 trigger events generated by Pythia were used and for measurement of MuFast efficiency we disposed of real data from collisions and minimum bias triggering.

Pythia is a set of algorithms for generation of high-energy physics collision, i.e. for the description of collisions at high energies between elementary particles such as e^+ , e^- , composite particles such as p and \bar{p} in various combinations. It contains theoretical prediction and models for a number of physics aspects, including hard and soft interactions, parton distributions, initial and final-state parton showers, multiple interactions, fragmentation and decay. It is largely based on the original research, but also borrows many formulas and other knowledge from the literature. For this study we have used one of the well-known decays, Z boson into two muons. This decay has the advantage of muons with high momentum, so trigger should be fired in every event. One of real events of this decay is shown in Figure 4.1.

Minimum bias events pass-through data quality selection criteria. This criteria are dependent on experiment settings and detector performance. For ATLAS the criteria used in our analysis are:

- at least 1 side MBTS hit (Minimum Bias Trigger Scintillator)
- a primary vertex, no pile-up, no mis-measured tracks
- at least 2 tracks with $p_T \geq 100$ MeV, $|\eta| \leq 2.5$

- at least 1 B-layer pixel hit 2, 4, or 6 SCT hits for $p_T \geq 100, 200, 300$ MeV, respectively. Cuts on the transverse (d_0) and longitudinal (z_0) impact parameters of tracks w.r.t. the primary vertex.

From these parameters it is easy to see that this cuts are sufficient to obtain relatively clean events without large losses.

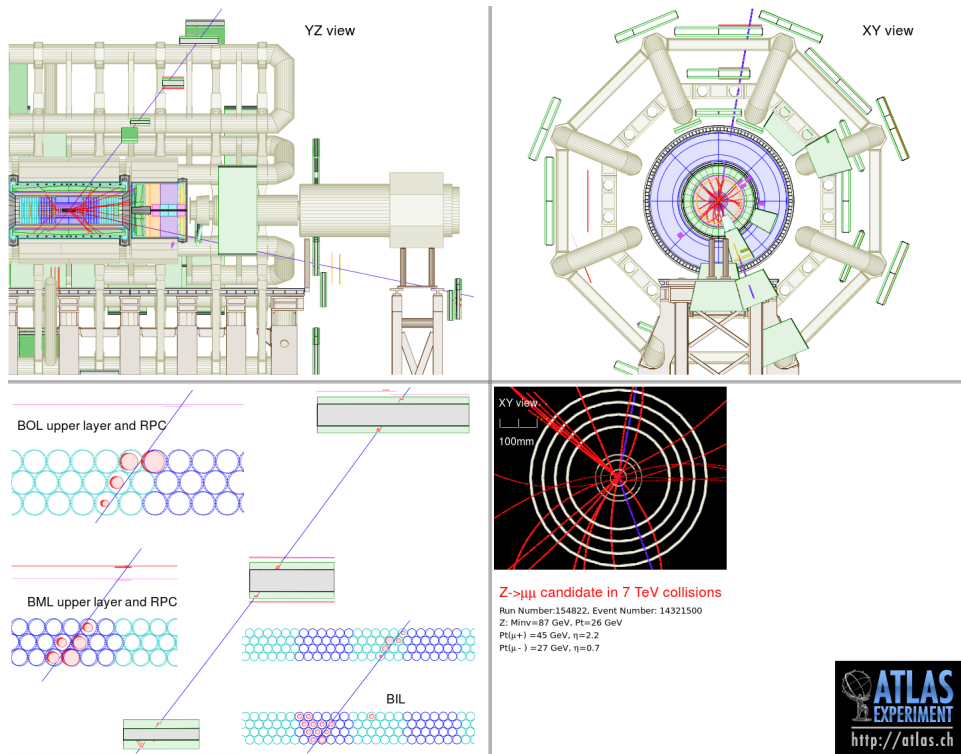


Figure 4.1: Candidate to $Z \rightarrow \mu^+ \mu^-$ decay from real ATLAS data[5].

4.2 Level 1 efficiencies

When we use MC generated and simulated events, we can choose which trigger menu to apply. We have chosen an early physics menu for luminosity of 10 to the power of 31. Muon LVL1 trigger items available in the early physics trigger menu are:

L1_MU4	L1_MU6	L1_MU10	L1_MU11
L1_MU20	L1_MU40	L1_2MU4	L1_2MU6
L1_2MU10	L1_2MU11	L1_2MU20	L1_2MU4_MU6

Number in the suffix of trigger identifier is transverse momentum threshold in GeV. For example L1_MU6 trigger will mark every event with a muon with a transverse momentum higher than 6 GeV. Furthermore, number in prefix of muon L1 trigger item as “2MU” implies number of muons with this threshold which are required in the event for it to pass. It is clearly visible that increasing the thresholds lowers the number of events that have passed. The trigger efficiencies are calculated by dividing the histograms of events with this trigger by histograms with all events that pass selection criteria.

4.2.1 Event distribution

Before efficiencies of triggers are computed, we will have a look at the observable quantities. First of them is momentum p (Figure 4.2). We can see that most of the muons have transverse momentum between 20 GeV and 80 GeV. That is why we have large error bars in efficiencies for p_T outside of this area (Figure 4.4 and 4.7). Another observable is pseudorapidity η of the track (Figure 4.3), it is symmetric and the most of muons have $|\eta| \leq 2.5$. That is given by the detector geometry.

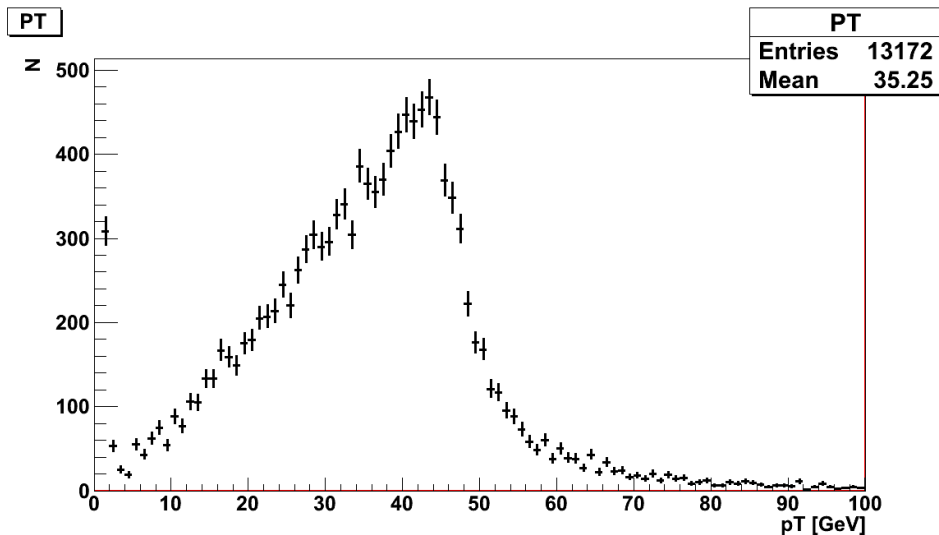


Figure 4.2: Distribution as a function of p_T for Monte-Carlo events for $Z \rightarrow \mu^+ \mu^-$.

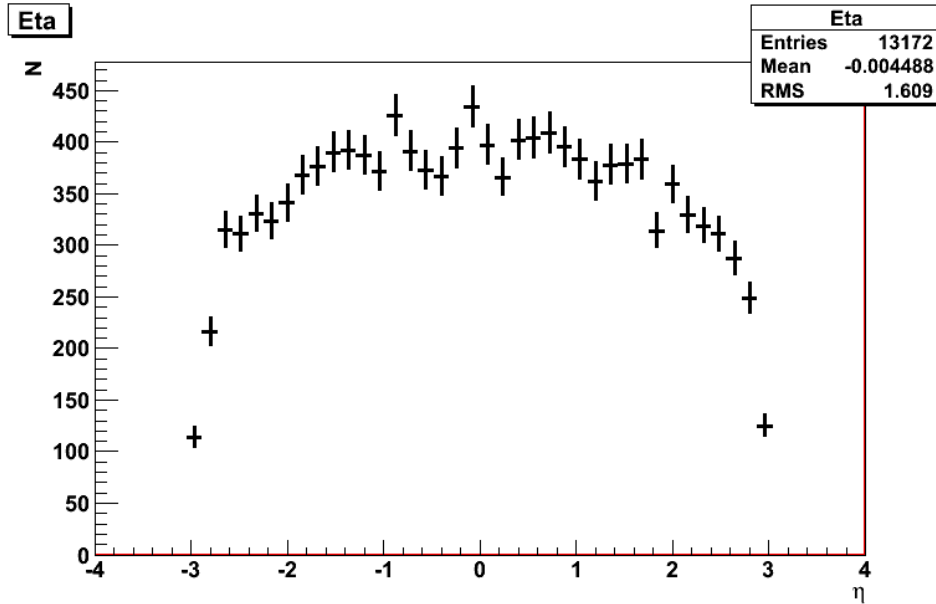
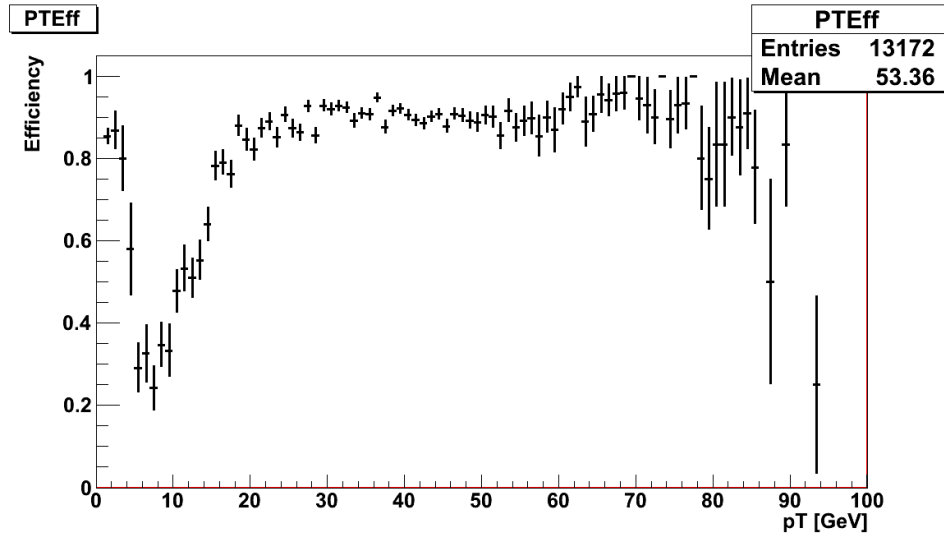
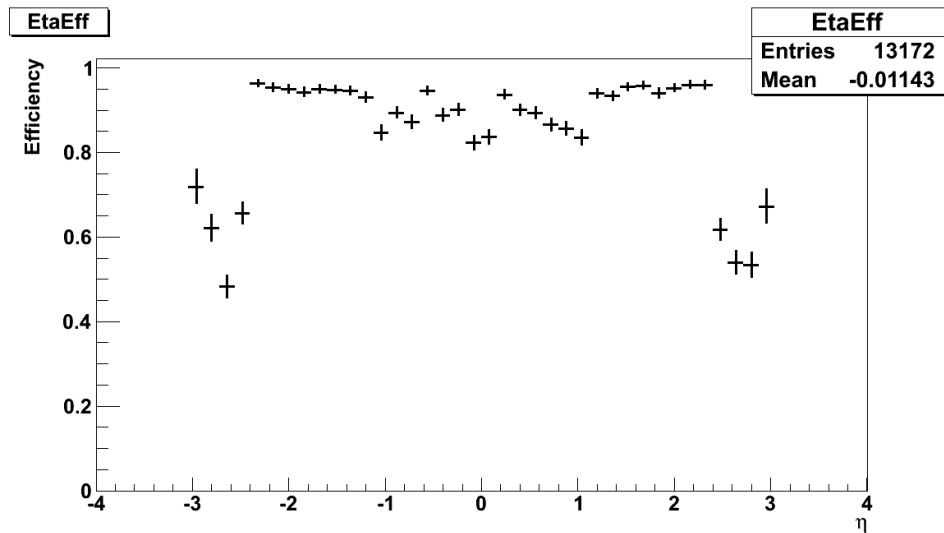


Figure 4.3: Distribution of events in pseudorapidity η for $Z \rightarrow \mu^+ \mu^-$ decay.

4.2.2 L1_MU20 item

This trigger demands that at least one muon in the event has transverse momentum at least 20 GeV. Muons with this energy are derivable from decays of particles with high invariant mass such as Z or W bosons or require a large Lorentz boost [4,5]. In Figure 4.4. we can see that efficiency is very close to unity for muons with momentum higher than 20 GeV. Events in energy range of 1 to 5 GeV are made by sorting collections in script, it was hard to resolve which muon in event was triggered so all of them were counted in. Next histogram (Figure 4.5.) shows how trigger efficiency depends on the pseudorapidity of muon track. We can see that it is symmetric and it has few pits around $\eta = 1$ and 0. It is caused by the detector geometry and around $\eta = 0$ it is caused by gap between RPCs on both sides. Hits from this plates can't be combined into the trigger tower. When we look at the Figure 2.6. (the Muon Spectrometer), we can see that at $\eta = 1$ RPC stations end and TGCs start and this is reason for the drop in efficiency. No particle track with pseudorapidity higher than 2.4 are created, this is due to termination of muon spectrometer chambers of the TPC type used for triggering at this pseudorapidity coordinates. The histogram of dependency on ϕ (Figure 4.6) shows that efficiency of the trigger isn't strongly dependent on ϕ .

Figure 4.4: Efficiency of L1_MU20 as a function of p_T .Figure 4.5: Efficiency of L1_MU20 as a function of η .

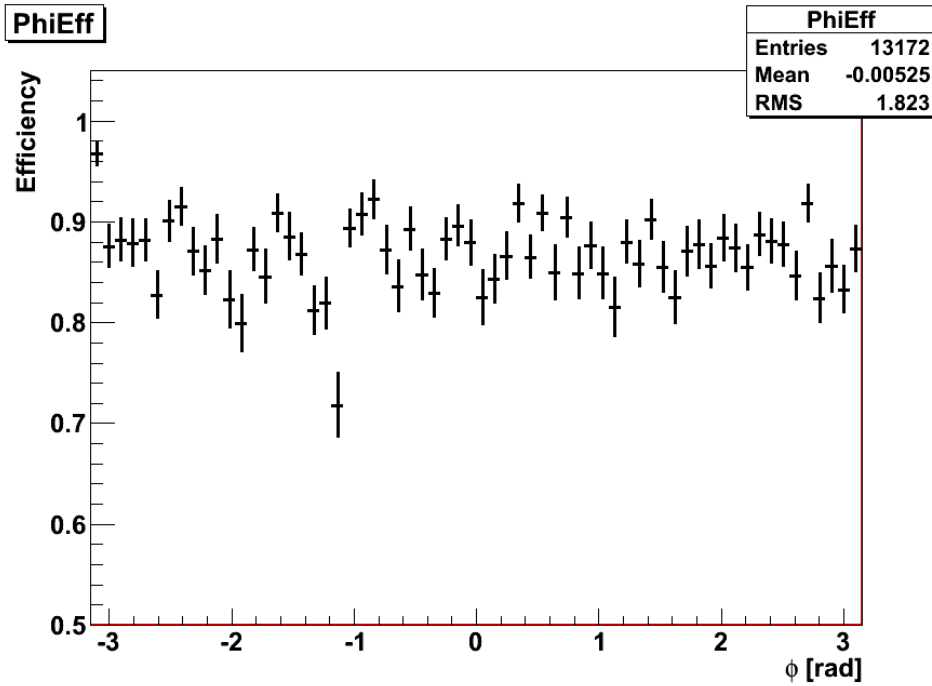
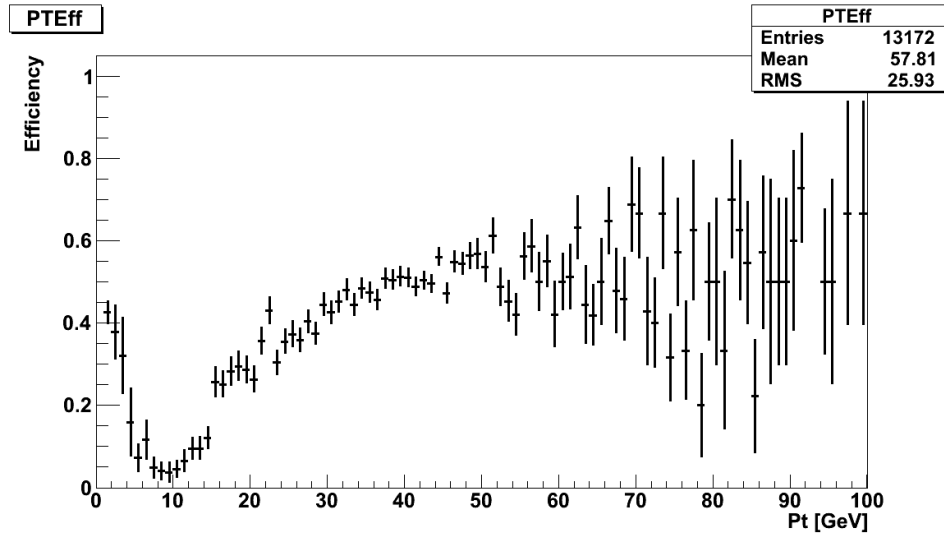
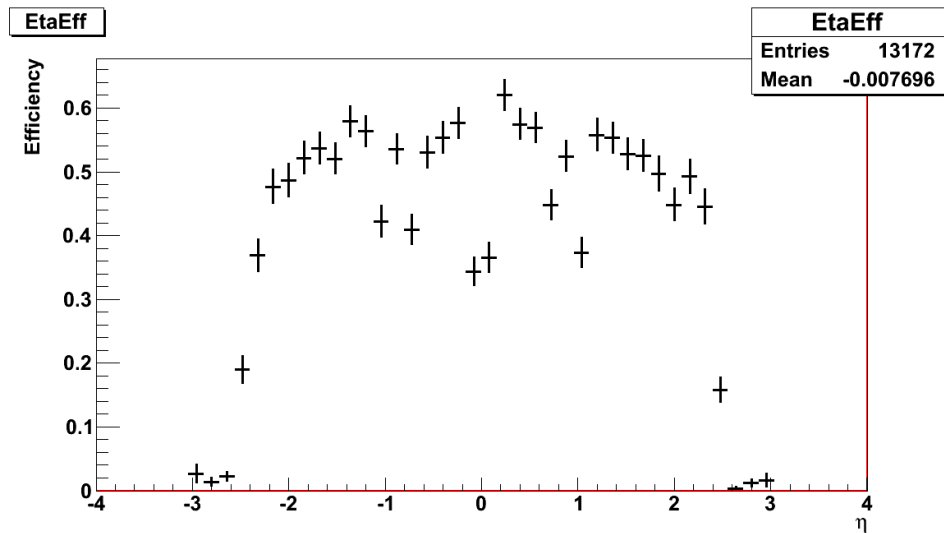


Figure 4.6: Efficiency of L1_MU20 as a function of ϕ .

4.2.3 L1_2MU20 item

This trigger has been studied to compare efficiencies of triggers and also for comparison between single and di-muons triggers. This trigger has the 20 GeV energy threshold for both muons. First thing to say about these efficiencies is that they are much smaller than for single-muon L1_MU20, that is because two good muon tracks are needed. There is a higher probability of not triggering both muons because of distribution of energy, detector angular cuts or misidentification. In L1_MU20 example we see that efficiencies are around 0.9, for di-muon case the trigger efficiency dropped to about 0.6. In Figure 4.6 we can see the dependence on transverse momentum. The first thing what we see is a small efficiency drop around 20 GeV caused by trigger threshold. We can compare it with same histogram for trigger L1_MU20, which we studied earlier (Figure 4.3) and the only difference is the value of efficiency. The other histograms show similar behavior for η and ϕ (Figure 4.7 and 4.8). In Figure 4.4. for single-muon case small drops in trigger efficiency are visible at around $\eta = 0$ and 1, in the case of di-muon trigger these drops are amplified due to the fact that trigger requires two triggered muons. In case one of the muons passes through this η area, chances that the trigger will not fire is much higher.

Figure 4.7: Efficiency of L1_2MU20 as a function of p_T .Figure 4.8: Efficiency of L1_2MU20 as a function of η .

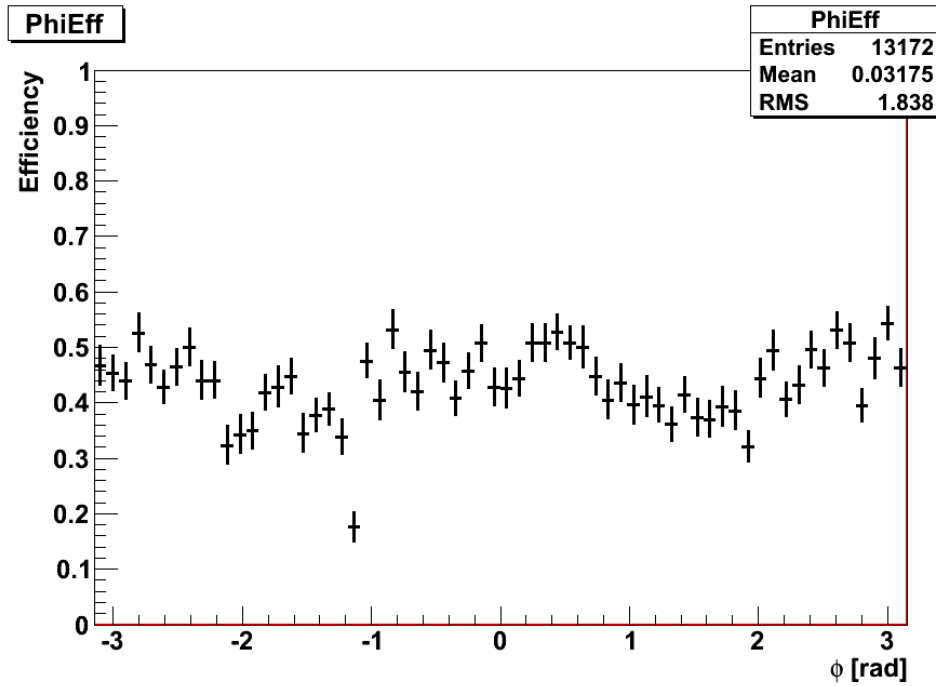


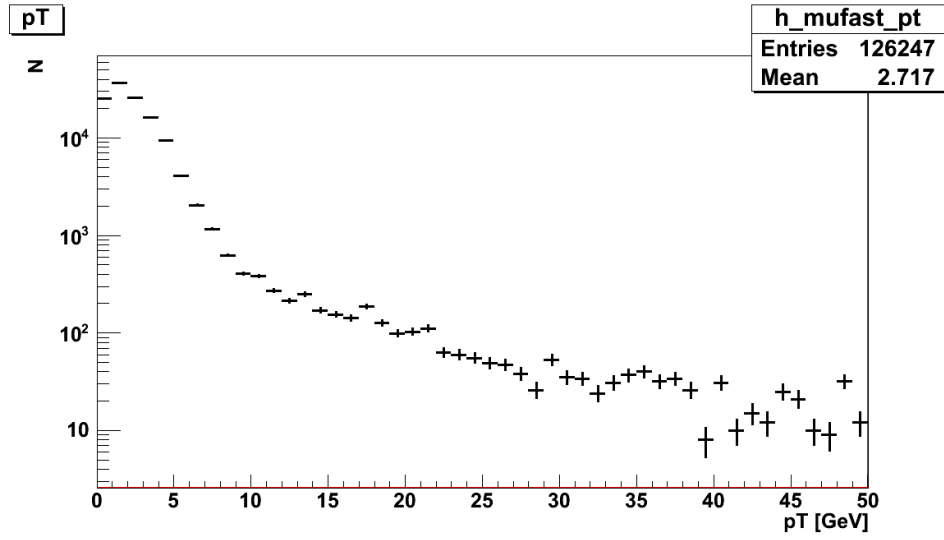
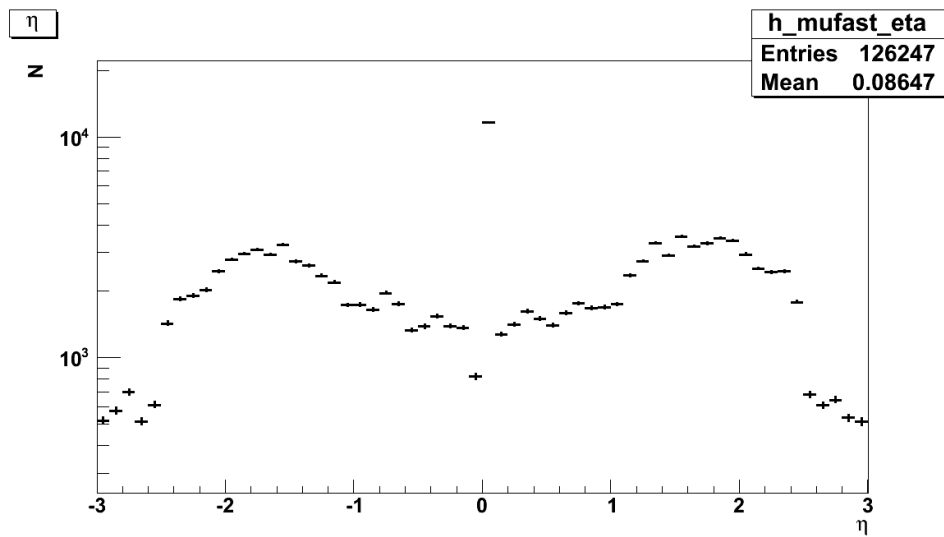
Figure 4.9: Efficiency of L1_2MU20 as a function of ϕ .

4.3 MuFast efficiency

Minimum bias data have some difficulties. One of them is small number of triggered events. In chapter 3 we said that the rejection factor of trigger is 10^7 , all of this is made by triggers decisions to refuse events which don't pass trigger threshold, in minimum bias we apply only few restrictions. But some of these restrictions are identical to the cuts which we need to apply for calculation of muFast efficiency. We only need events which fired LVL1 muon trigger. After this we have rejection factor 10^2 , that means that we can use one event from 100.

4.3.1 Event distribution

If we compare distribution of minimum bias events to events from Z boson decay (Figure 4.2) we clearly see that minimum-bias events have smaller average transverse momentum p_T . Other distributions are uniform with respect to LVL1 trigger decision. This means that they correspond to detector acceptance with one exception on $\eta = 0$ and $\phi = 0$. This coordinates are written for all events which fired LVL1 trigger but had no track parameters.

Figure 4.10: p_T distribution in minimum bias events.Figure 4.11: η distribution in minimum bias events.

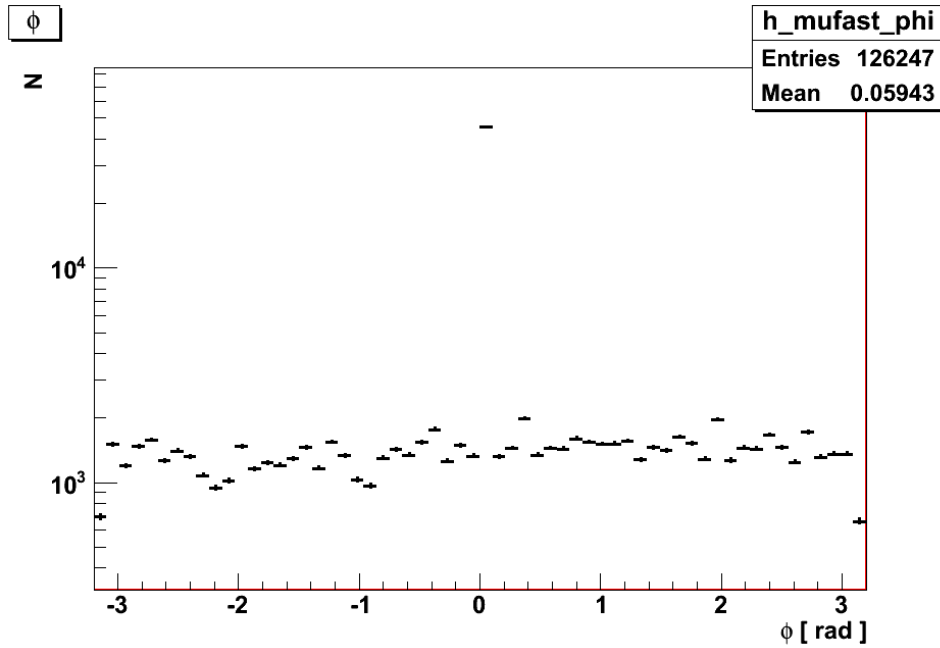


Figure 4.12: ϕ distribution in minimum bias events.

4.3.2 Efficiency of MuFast in dependence of LVL1 decision

Main task of MuFast trigger is to filter-out events with low p_T muons or with wrong identification. This is the reason why histogram of p_T distribution (Figure 4.13) shows that all muons with p_T higher than 5 GeV pass this trigger. Histogram of efficiency in dependence in pseudorapidity (Figure 4.14) shows that tracks in barrel $\eta \leq 1$ are better tracks with higher p_T . For $\eta \geq 1$ tracks have smaller efficiency, it is because ATLAS is using different type of muon chamber (TPCs). Gap in $\eta = 0$ is caused by wrong tracks identified by L1 trigger. We see two types of points, the black one is for events which fired L1_MU0 and the red one for events which passed L1_MU6. We see that for L1_MU6 muFast has higher acceptance than for L1_MU0 for tracks in end-caps. The difference of acceptance is much smaller in the barrel section. Histogram of efficiency (Figure 4.15) as a function of ϕ is about the same for both triggers, only L1_MU6 has higher efficiencies.

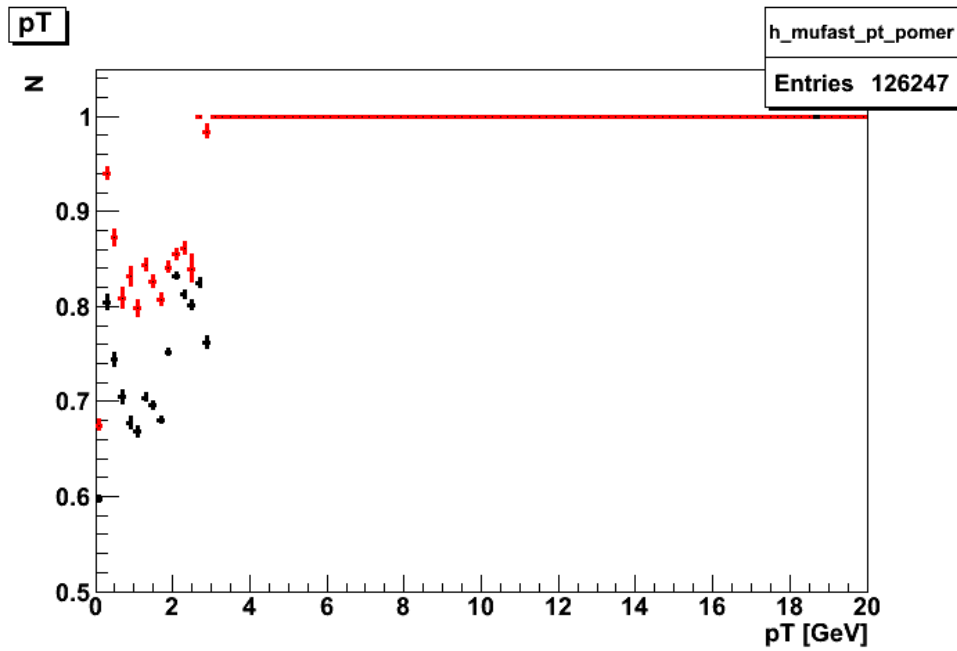


Figure 4.13: Efficiency of muFast trigger as a function of p_T for L1_MU0 (black) and L1_MU6 (red).

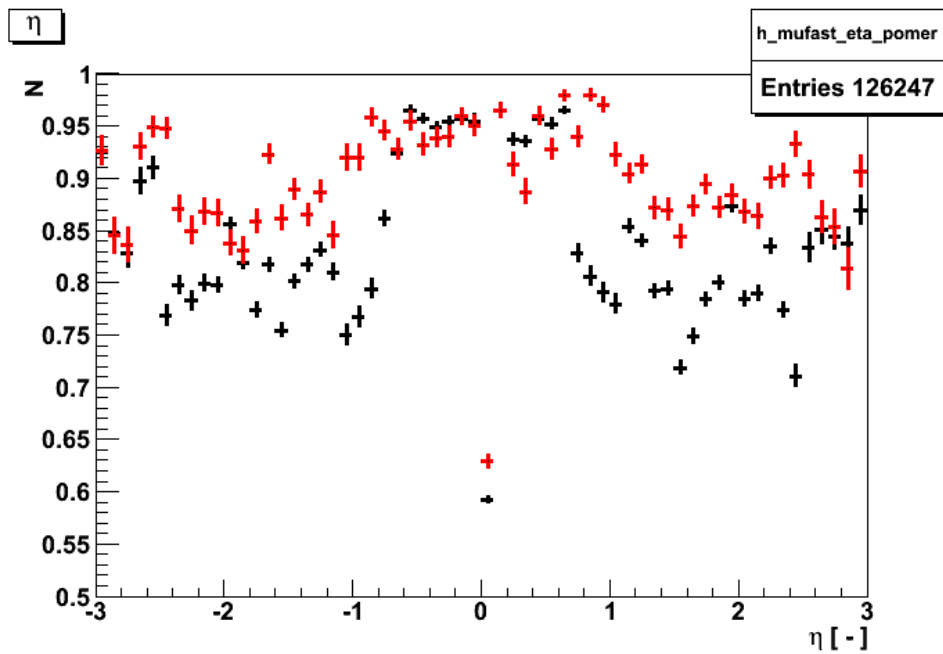


Figure 4.14: Efficiency of muFast trigger as a function of η for L1_MU0 (black) and L1_MU6 (red).

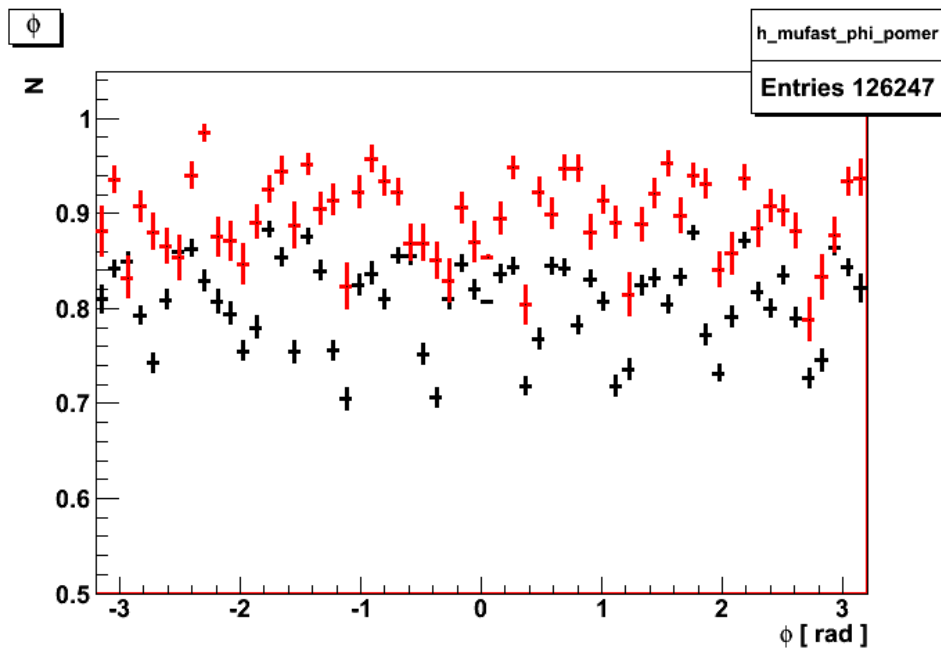


Figure 4.15: Efficiency of muFast trigger as a function of ϕ for L1_MU0 (black) and L1_MU6 (red).

Chapter 5

Conclusion

In this work the efficiencies of the selected LVL1 muon triggers and LVL2 muFast algorithm were discussed. In the LVL1 trigger system, two triggers were examined, namely L1_MU20 and L1_2MU20. In this case muons must have transverse momentum higher than 20 GeV in order to pass corresponding trigger thresholds. Single muon trigger has naturally higher efficiency than the di-muon trigger. We found that the LVL1 trigger works as expected and the efficiency reaches 85% for the single muon trigger and 50% for the di-muon trigger.

We found that the trigger efficiency rises up with the rising p_T , as expected. The dependence of efficiency on the pseudorapidity η and the azimuthal angle ϕ is uniform with exception of the transition region between the barrel and the end-cap. This particularity causes the drop in efficiency of the muon trigger at coordinates $|\eta| = 1$ and at $|\eta| = 0$.

When we study MuFast efficiency we found that it is about 100% for muons with $p_T \geq 3$ GeV and for muon with smaller transverse momenta is from 70% to 80% in dependence on LVL1 muon trigger decision, as expected. The efficiency of MuFast as a function of η is smaller in the end-caps compared to the barrel. We can conclude that ATLAS muon trigger is in a good shape and works as expected. It is ready to fulfill its duties in the 2011 data taking.

Bibliography

- [1] URL $\langle \text{http} : // \text{en.wikipedia.org} \rangle$, [cit. 2010-12-30].
- [2] PERKINS, D. Hill., Introduction to High Energy Physics. Cambridge university press, 4. edition, 2000.
- [3] HUANG, K., Quantum Field Theory, Wiley, New York, 1998.
- [4] MadGraph Version 4, URL $\langle \text{http} : // \text{madgraph.hep.uiuc.edu} / \rangle$, [cit. 2010-12-10].
- [5] URL $\langle \text{http} : // \text{atlas.ch} \rangle$, [cit. 2010-12-30].
- [6] ATLAS Collaboration, Expected Performance of the ATLAS Experiment, Detector, Trigger and Physics, CERN-OPEN-2008-020, Geneva, 2008.
- [7] ATLAS Collaboration, Magnet system technical design report, CERN-LHCC-97-018, 1997.
- [8] ATLAS Muon Collaboration, ATLAS Muon Spectrometer Technical Design Report, CERN-LHCC 97-22, May 1997.
- [9] CARADINI, F., The Level-1 Trigger Barrel System of the ATLAS Experiment at CERN, MUON-INT-2007-002, 2007.
- [10] MATTIA, A. Di, et al., Online Muon Reconstruction in the ATLAS Level-2 trigger system, ATL-COM-DAQ-2005-004, 2004.
- [11] ATLAS Collaboration, The ATLAS Experiment at the CERN Large Hadron Collider, 2008 JINST 3 S08003, 2008.
- [12] NAVON, S., ATLAS Muon Trigger for $pp \rightarrow \text{bbXJ}/\psi$ and $pp \rightarrow \text{XJ}/\psi$ Channels, CERN-THESIS-2008-061, 2008.

- [13] ATLAS Collaboration, "ATLAS Level-1 Trigger: Technical Design Report", CERN/LHCC/98-014, ATLAS-TDR-12, 1998.